



Ca' Foscari
University
of Venice

Masters' Degree
in Sustainable Chemistry and Technologies

Final Thesis

**DESIGN of SUPPORTED MONO and
BIMETALLIC NANOPARTICLES for
BIOMASS VALORIZATION THROUGH
TANDEM REACTIONS**

Supervisor

Ch. Prof. Maurizio Selva

Assistant supervisor

Ch. Dott. Daily Rodriguez Padron

Graduand

Francesco Zorzetto

Matriculation Number 869880

Academic Year

2022 / 2023

Table of Contents

1. Introduction

1.1. Biomass: definitions, composition, and valorization

1.1.1. Lignocellulosic, agricultural and forestry Biomass: statistics and generations

1.1.2. Food waste derived-biomass: fishery-waste rich in chitin.

1.2. Catalysis

1.2.1. Introduction to catalysis, and chitin as a precursor for N-doped carbonaceous materials

1.2.2. Synthesis techniques for supported catalysts synthesis

1.2.3. Catalysis in oxidation reactions

1.2.4. Catalysis in reductive amination reactions

1.3. Green Metrics

2. Experimental part

2.1. Material and equipment

2.2. Synthesis on supported metal nanoparticles on chitin derived N-doped materials

2.3. Material characterization

2.4. Typical oxidation reaction procedure and product analysis

2.5. Typical reductive amination procedure and product analysis

2.6. Typical tandem reaction procedure and product analysis

3. Results and discussion

3.1. Characterization of the heterogeneous chitin-supported metal catalysts

3.2. Catalytic activity

3.3. Influence of reaction parameters

3.4. Substrate scope

3.5. Catalyst reusability

4. Conclusions

5. Acknowledgments

6. References

1. Introduction

1.1. Biomass: definitions, composition, and valorization

Our current society heavily relies on the utilization of fossil resources, including coal, petroleum, and natural gas, for several crucial purposes. These resources play a pivotal role in meeting various critical needs, such as fulfilling energy demands and producing essential chemicals, materials, and fuels that are fundamental for the well-being of humanity.

According to US EIA's (Energy Information Administration) 2021 International Energy Outlook¹, if current policy and technology trends continue, global energy consumption and carbon dioxide emissions will increase through 2050 as a result of population and economic growth (Fig.1). To meet this demand, fossil resources will remain fundamental in our energy portfolio, albeit renewables are projected to account for 27% of our energy consumption by the year 2050¹.

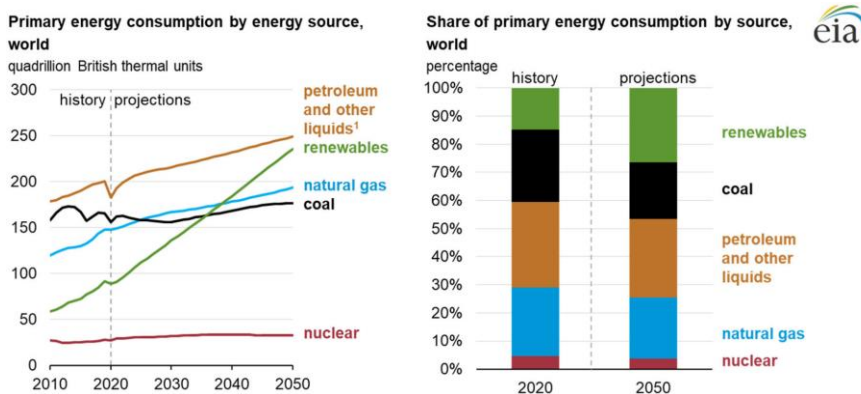


Fig. 1: on the left: Primary energy consumption by energy source in the world; on the right: share of primary energy consumption by source in the world; from IEO2021¹

While we can rely on many alternatives for energy production, one of the most promising options based on a renewable fixed-carbon sources is Biomass. The term Biomass is referred to any organic matter of both vegetable and animal origin that is available on a renewable basis compared to the human timescale. On lands above sea level, biomass derived from plants (~450 Gt C), often referred to as lignocellulosic biomass, is by far the most abundant one², amounting approximately to 150 billion t/y.^{3,4}

1.1.1. Lignocellulosic, agricultural and forestry Biomass: statistics and generations

According to the most recent FAO statistics (dating to 2021) almost 37% of total World land is used in agriculture⁵, while 30% is covered by forestry⁵. Biomass and its derivatives can be divided into 3 categories called “generations”:⁶

1. First generation feedstocks generally refer to products derived from plants rich in sugars (e.g. sugarcane, sugar beet, etc.), starches (e.g. corn, wheat, potatoes, etc.) and oils (e.g. olive, palm, sunflower etc.) and are used in the production of bioethanol and biodiesel (edible crops).
2. Second generation feedstocks primarily include products derived from non-food oil-rich plants and lignocellulosic biomass (inedible crops) and waste.
3. Third generation feedstocks comprise cyanobacteria and microalgae rich in lignocellulose, lipids and protein.

An exemplified scheme of this labelling is shown below in Fig.2.

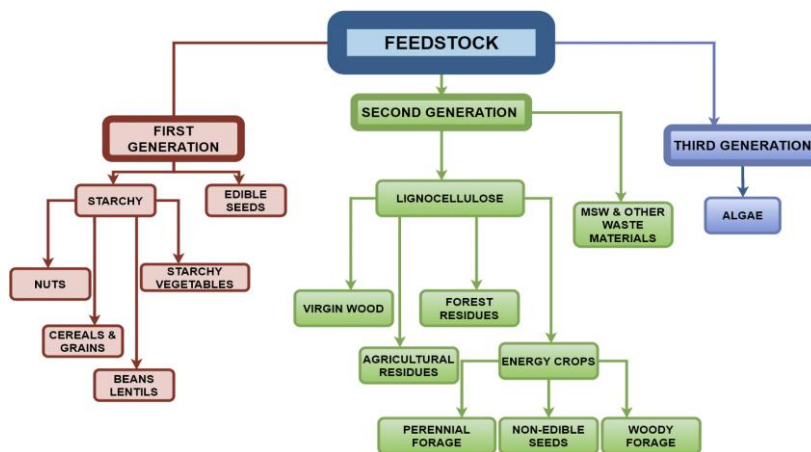


Fig. 2: exemplified scheme of biomass classification in 3 generations.⁷

The chemical composition of these feedstocks varies significantly, which in turn influences the choice of biomass conversion technologies required for each specific material. Additionally, there is an ethical concern regarding the utilization of edible crops for the production of fuels and chemicals. This issue becomes particularly pertinent when considering that in certain regions of the world, people still grapple with issues of hunger and malnutrition.

In addition to the pressing issue of hunger, projections indicate that by 2050, the world will need to boost food production by 50–70% compared to current levels.⁸ Consequently, it becomes evident

that utilizing food biomass as a feedstock in the biorefinery industry is an unsustainable strategy.

While many non-food crops also demand land for cultivation that could otherwise be employed for food crops, the most viable options among various sources are aquatic plants (third-generation biomass products) and second-generation biomass-derived materials. These include crop residues, forestry waste, purpose-grown grasses, woody energy crops, industrial byproducts, non-recyclable municipal solid waste, urban wood waste, and food waste.

Understanding the chemical composition of lignocellulosic biomass is crucial for the efficient production of fuels and chemicals. Biomass typically comprises three major components: lignin, cellulose, and hemicellulose (which includes starches, carbohydrates, sugars, and aromatics). Additionally, there are less abundant substances such as volatiles/extractives (including resins, lipids, essential oils, and others), as well as ash (comprising inorganic materials either naturally present or introduced anthropogenically).

Therefore, biomass is a far more complex matrix compared to petroleum and other fossil resources. Consequently, efficiently extracting and isolating products with both high yield and purity from biomass represents a significant and highly challenging task.

Lignocellulose, one of the most interesting fractions, makes up from 80% to 90% of all vegetable biomass⁹, and it is comprised of cellulose, hemicellulose and lignin (Fig. 3)⁷

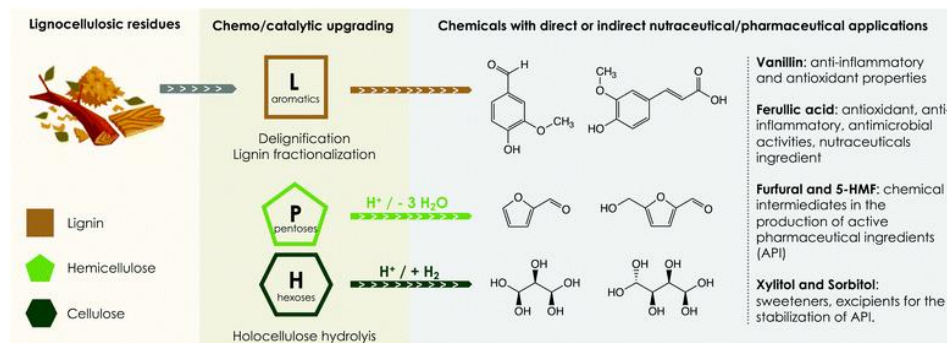


Fig. 3: Schematic representation of lignocellulosic fractions in vegetable biomass.

Cellulose is the most abundant biopolymer on Earth. More specifically, cellulose is a linear homopolymer of β -D-glucose with (β 1 \rightarrow 4) links which make it resistant to hydrolysis. Moreover, hemicellulose is an amorphous heteropolymer comprised of several different monosaccharides including C6-sugars (glucose, mannose and galactose) and C5-sugars (mainly arabinose and xylose). On the other hand, lignin is a three-dimensional, highly cross-linked macromolecule primarily

composed of aromatic alcohols, with the most common types being three substituted phenols: para-coumaryl alcohol, coniferyl alcohol, and synapyl alcohol. Lignin is intricately intertwined with the other components of cellulose and hemicellulose within the biomass structure, hence, representing a significant challenge in the processing of lignocellulosic materials.¹⁰ *Table 1* offers a more detailed picture of the composition of lignocellulose from different sources.

Table 1: Cellulose, hemicellulose and lignin content in five major lignocellulosic biomasses (% Dry Mass)¹¹

<i>Feedstock name</i>	<i>Cellulose</i>	<i>Hemicellulose</i>	<i>Lignin</i>
Wheat straw	31–39	22–24	22–24
Barley straw	33–40	20–35	8–17
Corn stover	39–42	22–28	18–22
Hardwood	40–55	19–40	18–25
Softwood	34–50	21–35	28–35

The physical and chemical behavior of the chosen feedstock will be different with respect to the original source and extraction method used. Therefore, its use in many applications may vary based on formulations.⁸ The composition of holocellulose, consisting of cellulose and hemicellulose, in lignocellulosic raw materials (LR) varies depending on the type of biomass, as shown in Table 1. This fraction can make up to 70% of the dry lignocellulose content. Holocellulose presents an opportunity as a sustainable reservoir of C6–C5 sugars, which can undergo subsequent conversion into a wide spectrum of molecules. These compounds are valuable renewable resources for the bio-based chemical sector and include acids, ethers, esters, alcohols/polyols, and furan derivatives.

Specifically, polyols obtained from cellulose and hemicellulose, such as sorbitol, mannitol, xylitol, and glycerol, find widespread use either as supplementary components or as active pharmaceutical ingredients (API) for instance for constipation. Their sweetness and dental-friendly attributes make them particularly suitable for this purpose. Moreover, furfural (FUR) and 5-hydroxymethylfurfural (5-HMF) are fundamental building blocks in various active compounds, including those aimed at managing hypertension, alleviating depression, reducing anxiety, and combating inflammation. FUR AND 5-HMF hold the potential to serve as feedstocks for the synthesis of bio-based pharmaceutical components and intermediates. Furthermore, lignin, the third major component of lignocellulose, boasts a sub-phenolic structure that allows for the production of lignophenols and lignans. These substances can be directly harnessed for their natural anti-inflammatory and antioxidant properties.

In addition, by employing appropriate depolymerization techniques, a plethora of aromatic precursors for bio-based APIs and pharmaceuticals can be readily generated.

Physical and/or chemical pretreatment methods are usually required, with a principal focus on accomplishing two primary goals: (i) disassembling the carbohydrate-lignin framework, and (ii) diminishing the crystalline nature of cellulose. Physical pretreatment techniques, such as milling, grinding, size reduction, and chipping, typically are aimed to increase the accessible surface area while concurrently reducing cellulose's polymerization extent and crystalline nature. Chemical pretreatments involve the use of substances such as acids, alkalis, salts, and organic/ionic solvents, which have been widely adopted to efficiently separate lignin and hemicellulose. Although these chemical pretreatments are conducted under mild conditions (room temperature and atmospheric pressure), environmental concerns arise regarding solvent recovery and reuse, particularly when strong acids/bases are employed. Thus, a combination of physico-chemical treatments (e.g., steam explosion, liquid/hot water, ammonia fibre/freeze explosion, CO₂ explosion, organosolv) is garnering increasing attention, even though they are generally costly on an industrial scale. In addition, biological pretreatments have been explored, but their applicability for large-scale chemical production remains limited due to their inherent sluggishness and lack of selectivity.

Pretreatment processes play a vital role in obtaining high-quality cellulose, hemicellulose, and sugars, often involving alterations to the native structure of lignin, which can otherwise severely impede further conversion. In this context, an effective approach for obtaining aromatic compounds from lignocellulosic resources is to initially convert the lignin fraction into propylphenols and phenylpropanols using processes known as reductive catalytic fractionation (RCF), also referred to as the "lignin-first" biorefinery approach.¹²

Considering such premises, throughout this Thesis, biomass-derived compounds were used as platform molecules for tandem reactions, with the aim of advancing biomass valorization towards the production of value-added products. Benzyl alcohol (BnOH) received the most extensive attention as substrate, since it is a naturally occurring monoaromatic alcohol with a broad range of commercial applications as fine chemical. It possesses low volatility and toxicity, yet strong polarity, being attractive as a safe and effective platform molecule whose derivatives find widespread use as flavors and fragrances in the cosmetics, pharmaceutical, and alimentary industries.¹³

During this project, different biomass-derived substrates were investigated beyond BnOH. These promising compounds are related to the US Department of Energy's (DOE) "Top 10" extensive work regarding the identification of the most promising biomass-derived compounds. In 2004,

Researchers from the US NREL (National Renewable Energy Laboratory), PNNL (Pacific Northwest National Laboratory) and Office of Biomass Program (EERE) conducted an extensive study to identify valuable sugar-based building blocks for lignocellulosic biomass.¹⁴ Starting from an initial list of over 300 candidates, criteria including the type of raw material, the estimated processing costs, the estimated selling price, the chemical functionality, the potential use and development in the market, etc., were established to identify 30 interesting chemicals (Figure 4, left). Thereafter, an additional selection process narrowed down the list of bio-based compounds to just over 10 molecules. This family of products was called the “top 10” and was released by the US DOE (Department of Energy) in the “Top 10” report, albeit in the final screening more than 10 target structures were present (Figure 7). In 2010, the “Top 10” list was revisited by adopting criteria which embodied technological and engineering aspects for high volumes of production, the existence of pilot plants, the occurrence of already recognized manufacturing processes, etc. This work still represents cornerstones in this field.

Identified Biobased Platform Chemicals	Typical Process	Challenges
Ethanol	Aerobic/Yeast fermentation	Established for first generation biomass; Hydrolysis required as pretreatment of second generation feedstocks; seasonal availability of sugar crops
Furans (Furfural, HMF, FDCA)	Acid-catalyzed dehydration of hemicellulose (furfural) or cellulose sugars (HMF), and oxidation (FDCA)	Low yields, high energy use, high mineral acid usage
Furans (Furfural, HMF, FDCA)	By-product of vegetable oil/animal fat transesterification or saponification (biodiesel or soap production)	Saturated market
Succinic acid	Anaerobic/Bacterial fermentation	Development of low cost fermentation routes, separation/purification of end product
Hydroxypropionic acid/aldehyde	Aerobic/Yeast fermentation	Low yields, fermentation pathway not known
Levulinic acid	Acid-catalyzed dehydration and decomposition of cellulose sugars/By-product of furan production	Low yields, high energy use, high mineral acid usage
Biohydrocarbons (isoprene)	Aerobic/Yeast fermentation	Cost of reaction vessels and compressors; availability of clean inexpensive bio-sugars
Sorbitol	Batch hydrogenation of glucose	Established technology, challenges in its conversion to high-added value derivatives.
Lactic Acid	Anaerobic fermentation	Lactic acid purification, use of second generation feedstocks
Xylitol/arabinitol	Hydrogenation of xylose/arabinose or biotransformation (steam pretreatment of lignocellulosics processing)	No technical challenges in hydrogenation. Biotransformations suffer from product separation. Challenges in its conversion to high-added value derivatives.

Fig. 4: Selection of the “Top 10” bio-based platform chemicals through the work commissioned by US DOE.^{14, 15}

1.1.2. Food waste derived-biomass: fishery-waste rich in chitin.

In addition to lignocellulosic agricultural and forestry residues, biomass derived from food waste could also serve as a compelling feedstock for the biorefinery industry (see Figure 5). According to the Food and Agriculture Organization (FAO) of the United Nations, an estimated 45% of the food produced is lost or discarded both before and after it reaches consumers. This accounts for over 1.3 billion tons of food annually, intended for human consumption globally. Food waste, rich in nutritional content, decomposes over time, creating favorable conditions for disease-causing

microorganisms to proliferate. Addressing this environmental concern involves reducing the generation of food remnants, but the most sustainable approach involves repurposing these residues for alternative uses and applications.

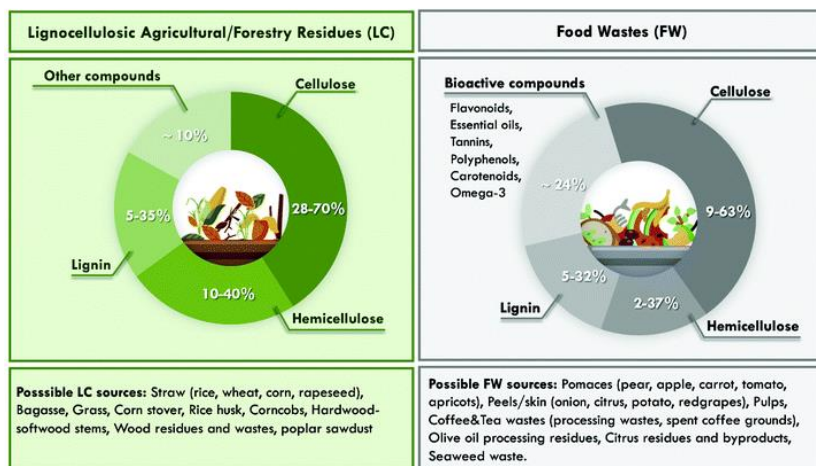


Fig. 5: Comparative composition of lignocellulosic agricultural/forestry residues and food wastes derived biomass.

Specifically, the volume of discarded materials originating from worldwide fisheries has been estimated, according to some analyses, indicating figures surpassing 20 million tons on an annual basis. This amount is roughly equivalent to approximately 25% of the total production, encompassing by-catch (non-target species) and waste generated during fish processing. On the contrary, other studies employing a 'catch reconstruction' method, which incorporates data not present in official FAO reports, indicate that global discards reached a peak of 18.8 million tons in 1989 and have since gradually declined to around 10 million tons per year.¹⁶

Despite the ongoing uncertainty surrounding the accuracy of statistics and estimates, it is evident that the annual volume of fish biowaste is substantial, reaching tens of millions of tons. This represents an incredibly valuable resource in terms of its chemical richness, which undoubtedly warrants exploitation and utilization.

Chitin is the second most abundant biopolymer on Earth after cellulose, but albeit its applications are desirable to design sustainable protocols, they are often hindered by its low solubility in most medias except task-specific ionic liquids.¹⁷ Chitin is a polysaccharide similar to Cellulose, as its comprised of 2-acetamido-2-deoxy- β -D-glucose (NAG or N-acetylglucosamide) monomers chained with $\beta(1\rightarrow4)$ linkages¹⁸ (Fig. 6).

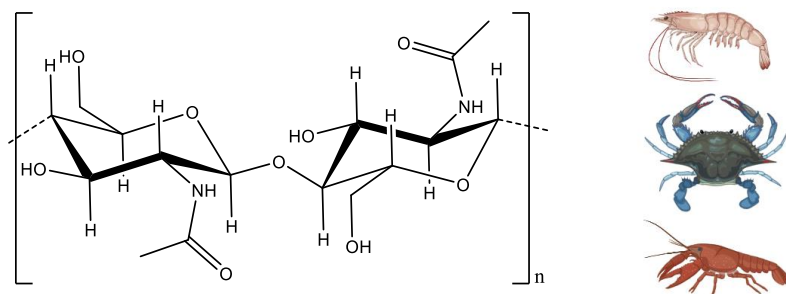


Fig. 6: Chitin polymeric structure and food sources rich in chitin.¹⁹

Chitin is the primary structural component of invertebrate exoskeletons and fungal cell walls.¹⁴ Its biodegradation is exceedingly slow, leading to concerns about its accumulation, particularly from the waste produced by the food industry, such as chitin waste from fishery processing. In the USA, between 50% to 90% of the solid waste comes from shellfish processing discards, contributing to a global annual estimate of approximately 5.1×10^6 metric tons.¹³ Therefore, the production of value-added products using chitin or its deacetylated form, chitosan, is of utmost interest, as they exhibit significant potential across a wide range of industrial applications.

Considering these premises, this project focuses on utilizing chitin obtained from fishery wastes as both a carbon and nitrogen source to produce *N*-doped carbonaceous materials. These materials have the potential for applications in catalysis for the conversion of biomass-derived platform molecules. Throughout this research, we accomplished the comprehensive utilization of biomass, extending to the transformation of solid fishery waste-derived chitin into carbon *N*-doped materials. These materials hold promise as supports in heterogeneous catalysis for the further upgrading of biomass-derived platform molecules used as substrates, such as benzyl alcohol (BnOH).

1.2. Catalysis

1.2.1. Introduction to catalysis, and chitin as a precursor for *N*-doped carbonaceous materials

Catalysis has undoubtedly established itself as a pivotal instrument in the realm of Green Chemistry, serving as a means to prevent pollution, enhance efficiency, improve yield, and refine selectivity. In fact, it plays a vital role in over 90% of contemporary chemical processes.²⁰

Numerous technologies devised in the petrochemical industry incorporate the use of solid catalysts as a crucial step, and this pattern is anticipated to persist in numerous biorefinery processes. Nevertheless, as illustrated in Figure 7, due to the distinct chemical compositions of fossil resources

and biomass, they cannot be treated with the same catalytic approaches.²¹

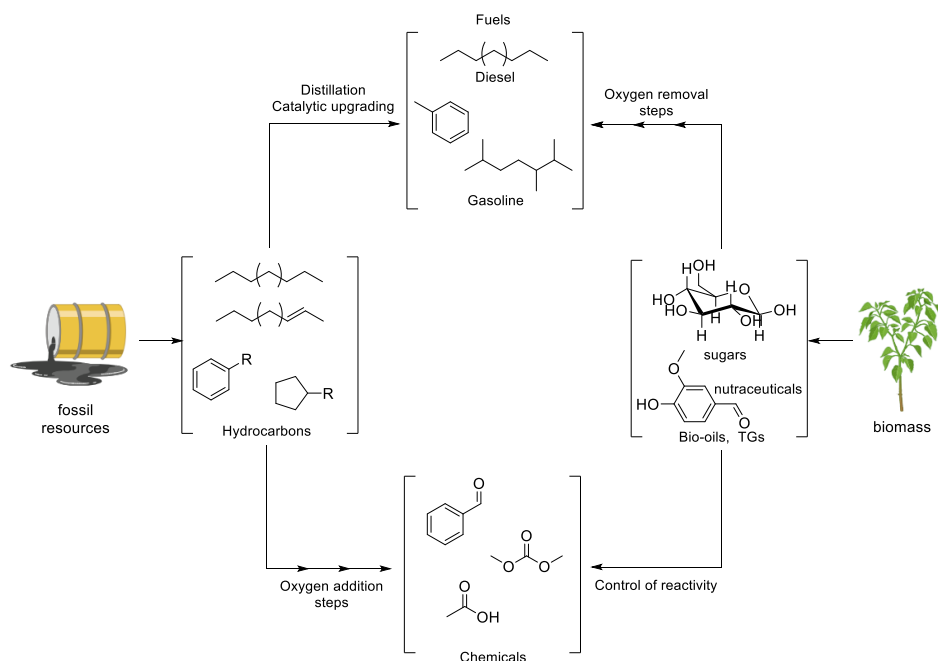


Fig. 7: Exemplified comparative processing approaches of petroleum and biomass to chemicals and transportation fuels.²²

On average, conventional biomass feedstocks tend to feature a substantial presence of oxygenated groups, whereas fossil resources are notably less functionalized. Consequently, the primary challenge lies in the development of novel catalytic materials and pathways that enable precise control of the heightened reactivity found in biomass feedstocks. This control is essential for directing synthesis toward target chemicals with both high selectivity and yield.

The challenges associated with these processing demands will significantly influence catalyst design. Over the past few decades, solid catalytic materials have been engineered to display improved efficiency and durability in gaseous phases, as well as to withstand hydrophobic conditions and high temperatures (necessary for activating fossil feedstocks). Inorganic oxides like alumina and silicates have proven to be exceptionally well-suited for these purposes and thus serve as the foundation for the majority of catalysts currently employed in the petrochemical industry.

In biomass sources, the oxygen-rich compounds present low volatility, suggesting that many biorefinery processes will be carried out in the liquid phase. Furthermore, high temperatures

(typically over 850°C in the petrochemical industries) are not necessary, both because of high reactivity and low thermal stability of the biomass feed. Consequently, appropriate catalysts for biomass conversion should be stable under liquid phase conditions and be particularly resistant to leaching.¹⁷

In this context, the development of efficient, selective, and enduring catalytic systems emerges as a significant challenge. Heterogeneous catalysts, in particular, hold a distinct advantage due to their ability to be readily separated from the reaction mixture. This characteristic not only minimizes waste generation but also aligns with the fundamental principle of green chemistry, which emphasizes waste prevention. Consequently, in the realm of green chemistry, heterogeneous catalysis is typically preferred over homogeneous catalysis. This preference underscores the prominent role of heterogeneous catalysis in a biorefinery setting compared to homogeneous catalysis.²³

Additionally, heterogeneous catalysts are usually less expensive and allow for better recycling, truly matching Green Chemistry principles. General properties about homogeneous and heterogeneous catalysis are listed in *Table 2* below.

Table 2: *General properties of homogeneous and heterogeneous catalysts.*^{21, 21, 24}

Criteria	Homogeneous cat.	Heterogeneous cat.
diffusion problems	almost absent	controlled by mass transfer
reaction conditions	generally mild	generally severe
thermal stability	low	high
recovery	often complicated and problematic (catalyst degradation)	very simple
recycling	possible	very simple
loss of material cost	high	low

Unlike silica-aluminates (typically employed in the petrochemical industries), carbonaceous materials exhibit good stability in liquid conditions and high resistance to chelating and acidic media, which generally makes them optimal supports for biomass catalytic conversion.

Furthermore, biorefinery transformations typically involve multistep processes aimed at converting biomass into fuels and chemicals. Therefore, there is a need to develop multifunctional materials capable of catalyzing multiple reactions within the same catalytic bed. This approach would streamline system complexity.¹⁷ Carbonaceous supports are ideal in this respect, since depending

on the chosen biomass feedstock, it is possible to confer specific functionalities to the desired materials.²⁵ They also present outstanding physicochemical properties, such as high specific surface area, pore volume, excellent electric and thermal conductivity.²⁶

To enhance the metal-support interactions in supported metal catalysts, one highly effective approach involves the introduction of heteroatoms, such as Nitrogen (N), into the carbonaceous materials. This serves to disperse and stabilize the supported metal nanoparticles (NPs), resulting in significant alterations to the materials structure and catalytic performance. It is important to note that the specific effects observed depend on the type of nitrogen incorporated into the carbonaceous material: we can distinguish graphitic N (N_g), pyrrolic N (N_{pl}) and pyridinic N (N_p) (Fig. 8) based upon their different interactions with metal NPs.

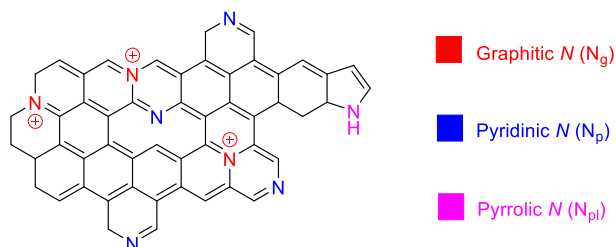


Fig. 8: graphitic N (N_g), pyridinic N (N_p) and pyrrolic N (N_{pl}) are depicted in the picture in an exemplified N-doped carbonaceous material.

Recent studies established indeed that the difference lies in that N_g , as well as N_{pl} , do not bond to metal NPs directly, whereas N_p does. This is justified by the repulsion between N_g and NPs from the donating character of electron-rich N_g atoms in the p_z orbitals, which prevents electron transfer from NPs to N_g (also observed in the case of N_{pl}). Accordingly, the strong d-p bonding interaction between NPs and N_p can be attributed to the electron withdrawing ability of N_p .²³ These characteristics suggest that graphitic nitrogen (N_g) can facilitate the nucleation and dispersion of the active phase, whereas pyridinic nitrogen (N_p) serves a dual role as an anchor and dispersant for metal nanoparticles (NPs).²³ Pyrrolic N (N_{pl}) interacts with metal NPs similarly to N_g and is a weaker active base-site than pyrrolic N (N_p) sites.²⁷

Drawing inspiration from this inherent value, this study encompassed the development and characterization of metal-based heterogeneous catalytic nanomaterials designed for tandem reactions. These materials were synthesized using chitin as a carbon and nitrogen source, ultimately yielding N-doped carbons, which could 1) lead to the generation of new active sites for base-catalyzed reactions (not employed in this work, albeit it represents an interesting attribute) and 2)

promote the well-dispersion of the metal entities in the support, influencing both catalytic response and incorporation of metallic precursors thanks to the metal-nitrogen interactions in the investigated materials¹³ (a schematic representation of the functionalization is shown in Fig. 9). The bonding interactions between the metal nanoparticles and the pyridinic N functional groups, which are present on the chitin-derived support, significantly contribute to preventing the leaching of the active phase.

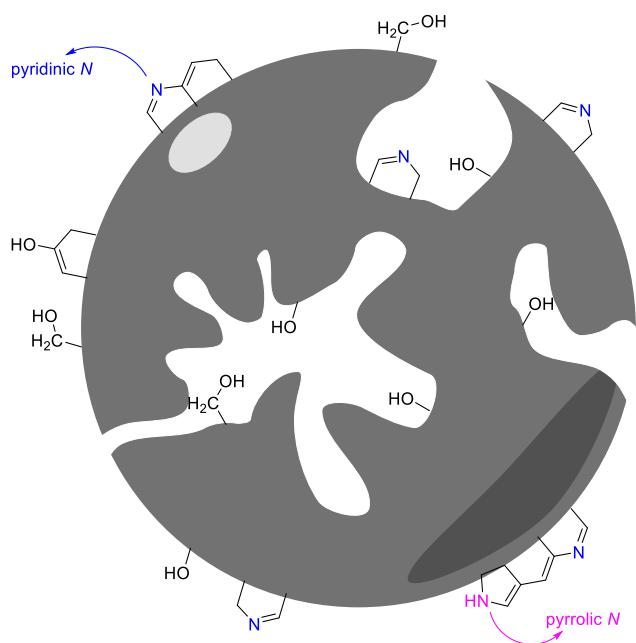


Fig. 9: schematic representation of the superficial functionalization with pyridinic N, pyrrolic N in the N-doped carbonaceous materials obtained from chitin.

The literature describes the preparation of N-doped materials (N/C) from different starting N-containing polymers, either bio-based such as chitosan,²⁸ or of fossil provenance as polyvinylpyrrolidone.²⁹ By utilizing chitin instead, we can circumvent the deacetylation process required to produce chitosan, all while maintaining the eco-friendliness of a bio-based material. It is crucial to highlight that while there is a strong desire to explore innovative applications of chitin to establish sustainable processes, these endeavors often face substantial obstacles, primarily stemming from chitin's limited solubility. Therefore, the pursuit of new avenues for the valorization of chitin remains highly desirable.

1.2.2. Synthesis techniques for supported catalysts synthesis

Supported catalysts consist of an active phase dispersed on a carrier. The properties of the catalytic materials can be controlled through the choice of the preparation method. The most common processes are impregnation, ion-exchange, adsorption, and deposition-precipitation techniques.³⁰

Impregnation is the procedure by which a certain volume of solution containing the metal precursor is mixed with the solid support, which is then dried to remove the solvent. Impregnation can be performed through two different set of conditions: wet impregnation, where an excess of solvent is used and then removed by drying; incipient wetness impregnation, where the volume of solvent used is equal or slightly less than the pore volume of the support. In both cases, temperature is a crucial factor, as it impacts both solubility of metal precursors, and the solution's viscosity. The maximum loading is also limited by the solubility of the precursor in the chosen solvent.

Ion exchange consists of replacing an ion through an electrostatic interaction between the surface of a support and another ion species. It's a variation of impregnation, as the supports (containing ions labelled as "A") is submerged in a solution with ions labelled as "B". Ions B gradually penetrate the pores of the support, while ions A transfer to the solution.

Adsorption allows the controlled anchorage of the precursor on the support in an aqueous solution. Ionic species are attracted electrostatically by charged sites on a solid surface.

Deposition-precipitation involves 3 steps: oversaturation, nucleation, and growth of the crystals. As depicted in the Fig. 10, the solubility curve of a solute depends on temperature and pH of the solution. We can then identify 2 regions: the region of stability of the precipitate and the region of stability of the solution. The oversaturation curve delimits an area of the graph, where liquid phase is still possible, but the solute precipitates when incurring in perturbation phenomena. This region is reachable through concentration variations, from B to C through solvent evaporation, or from B to A through rising the temperature. It is also possible to go through these different phases changing the pH.

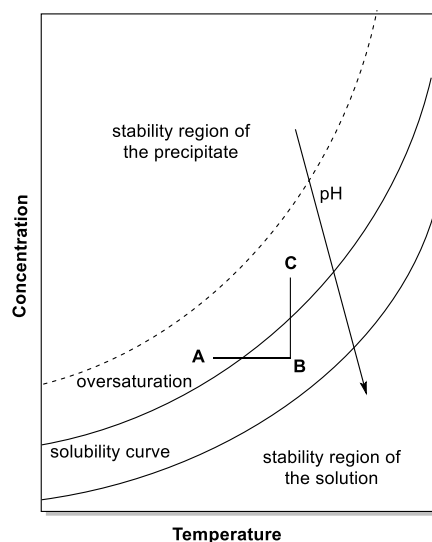


Fig. 10: depiction of described processes happening during oversaturation of a solution through precipitation-method of preparation for heterogeneous catalysts.

In the oversaturation stage, nucleation and growth of crystals happen. Nucleation can happen spontaneously (homogeneous nucleation), or it can be induced with crystallization seeds able to sprout nucleation in the material.²⁷

The impregnation method possesses numerous advantages, especially from an environmentally point of view, considering the minimal amount of solvents used. However, it presents some drawbacks, such as lack of homogeneity and the low control of particle size and dispersion. Regarding the solution (deposition-dispersion) method, it generally allows a better control on the morphology, dimensions and dispersion of the yielded nanoparticles in comparison to the impregnation strategy.³¹

Throughout the course of this research, the method chosen for catalyst preparation involved solution-precipitation techniques. This approach was selected because it had been thoroughly investigated and proven successful in prior studies of our research group related to the topic.^{29, 15} It will be further discussed in the “materials and methods of preparation” section of this thesis.

Mechanochemistry has emerged as a promising synthetic protocol to produce new materials.³² It is an environmentally friendly approach, which has still underexplored potential in spite of being a technique used since prehistoric times.^{33, 34}

Mechanochemistry refers to chemical reactions induced by mechanical energy, which is known to cause wear and tear due to friction, stress and strain on a large scale, and at molecular level, where this energy can cause reactions in the solid-state by shear stress, breaking symmetry destabilizing chemical bonds, making them prone to react.

Currently there are numerous techniques, previously discussed, to prepare metal nanoparticles involving solvents. Mechanochemistry avoids, or strongly limits, the employment of solvents during the synthesis steps, making it an interesting strategy, as it would benefit synthetic pathways in multiple ways: i) solvents have a big impact on the environment, as they often present low boiling points for an easy separation, so they can be easily dispersed, creating pollution or bring ozone-layer depletion. ii) solvents can linger as traces in the final products, potentially proving to be hazardous for human health, detrimental for product quality, or proving to be impurities or poisons for further processing of the product, thus bringing forth the necessity to regulate their residual traces, resulting in economic costs. iii) They can interfere with the process itself, creating parasitic reactions, limiting productivity.³⁰ Mechanochemistry is predominantly advantageous when used in reactions between solids that are not soluble, reactions in which solvents can negatively impact the process efficiency, and for yielding products in which solvents traces are a safety hazard.³²

Mechanochemical strategies can be employed both in batch conditions and continuous flow conditions: with ball milling devices that can be broadly classified into shakers or planetary mills (A and B respectively in *Fig. 11*); and with extruders, respectively (*Fig. 12*).³²

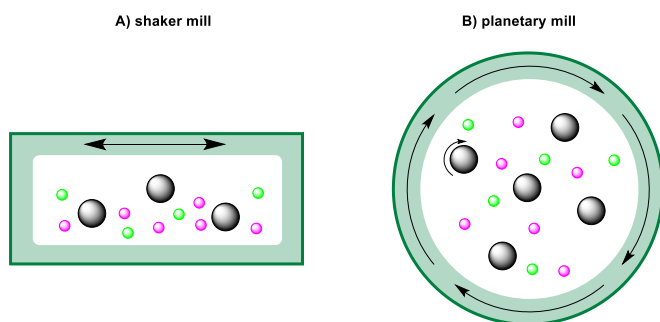


Fig. 11: schematic depiction of A) a shaker mill and; B) a planetary mill.

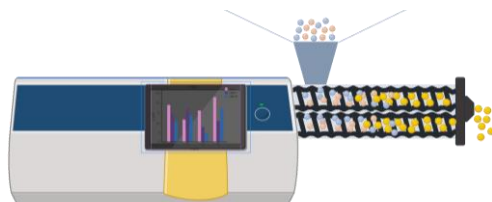


Fig. 12: schematic representation of a twin-screw extruder.

In *shaker mills*, the reactors are loaded with ball bearings and shaken at a desired frequency to grind reagents together. In *planetary mills*, the vessel spins at high speed in a counter direction to the spinning disc mounted on them. *Twin-screw extrusion* uses two counter-rotating screws to grind and transport the reagents through the tool's barrel. The reactions taking place in these devices involve dispersing force and mechanical activation which occur as a statistically probable processes according to collision theory.³⁵

Importantly, when engaging in mechanochemical protocols for catalyst synthesis, the key reaction parameters are controlled by: i) the milling time, ii) the nature of the milling action (*i.e.* the presence of either shear, impact forces, or both), iii) the milling energy (as in mechanical energy transferred to the reaction media), creating temperatures gradients and lowering the energy barrier for chemical reactions, and iiiii) the milling atmosphere.³² Effects of mechanical force on solids also include: i) milling-induced structural changes, ii) reduction in crystal size, iii) defects formation, iii) oxidation/vacancy creation. Mechanochemistry offers different grinding techniques, such as liquid-assisted-grinding (LAG), vapor-assisted grinding (VAG), ion and liquid-assisted grinding (ILAG) and polymer-assisted grinding (POLAG).³²

In the final section of this work, the use of mechanochemical protocol was explored for catalyzed organic transformations, employing a twin-screw extruder in continuous flow and solvent-free conditions.

1.2.3. Catalysis in oxidation reactions

The carbonaceous materials described above have versatile applications in various catalytic processes, including the oxidation of alcohols to carbonyl compounds. This particular transformation has garnered significant attention due to the growing interest in developing catalytic aerobic oxidation methods.

A variety of approaches with different catalysts and oxidizing agents have been proposed in the

literature, for such reactions. Peroxides, especially hydrogen peroxide and t-butyl hydroperoxide, molecular oxygen or air have been quoted as oxidizing agents.¹⁵

Oxygen is an excellent oxidant thanks to its abundance and its atom-economical transformations as well for the reason that its environmentally benign compared to other oxidants.³⁶ However, when used as pure molecular oxygen it represents a safety hazard for explosion risks, and it also is an expensive reagent. Instead, the use of air (the oxygen content in atmospheric air is 21% on average)³⁷ deserves recognition for its cheapness and safety, thus being an excellent choice for its employment in oxidation reactions. The oxidation of benzyl alcohol (BnOH) to benzaldehyde stands out as a highly appealing option within this category of reactions. This is not only due to the fact that BnOH is derived from biomass, but also because of the inherent value addition achieved by producing benzaldehyde, a versatile synthetic intermediate widely employed as a flavoring agent.¹³ An in-dept analysis on the available catalysts was made. Permanganate and chromate-based systems, endangered noble-metals and biocatalytic pathways have been often mentioned in the literature.¹⁵ Although these options often offer excellent synthetic results, major issues are associated with: i) difficult reaction scalability due to the limited availability and high price of noble metals, ii) the toxicity of the active elements (Mn and Cr) that poses a threat for human health and the environment, and iii) the storage, stability, and difficult reusability of enzymes.¹⁵

Other protocols have been devised for the oxidation of primary/benzyl alcohols, such as the employment of transition metal-based catalysts as Molybdenum supported on Metal Organic Frameworks (MOFs),³⁸ the use of co-catalysts based aminoxyl radicals (e.g. 2,2,6,6-tetramethylpiperidin-1-oxyl, shortened in "TEMPO"),³⁹ or bimetallic catalysts.¹⁵ Recent alternatives include the synthesis of carbocatalyst in the form of nano-sized materials, such as carbon nanotubes (CNTs). They have been used to activate a common oxidant (peroxymonosulfate, PMS) producing benzaldehyde from BnOH with selectivity and yield of 83% and 57% respectively, at 50 °C.⁴⁰

Inspired by these models, this study indeed represents a section of a far-reaching project during which different materials were tested with low-loading of Nickel, Iron, Cobalt and Molybdenum in the oxidation of benzyl- and furyl-type alcohols with emphasis on Molybdenum-*N*-C materials for the oxidation of BnOH to benzaldehyde.¹⁵

1.2.4. Catalysis in reductive amination reactions

The ultimate goal of this research encompasses the sequential reductive amination of the aldehydes generated during the oxidation step, all without the necessity to alter the catalytic bed. This entails

the development of a reaction environment and catalytic materials capable of efficiently facilitating two distinctly different transformations.

Reductive amination is described as the reaction between aldehydes or ketones with either ammonia, primary amines, or secondary amines in the presence of a reducing agent to give primary, secondary or tertiary amines.⁴¹ The general reaction pathway of a reductive amination reaction is reported in the Fig.13.

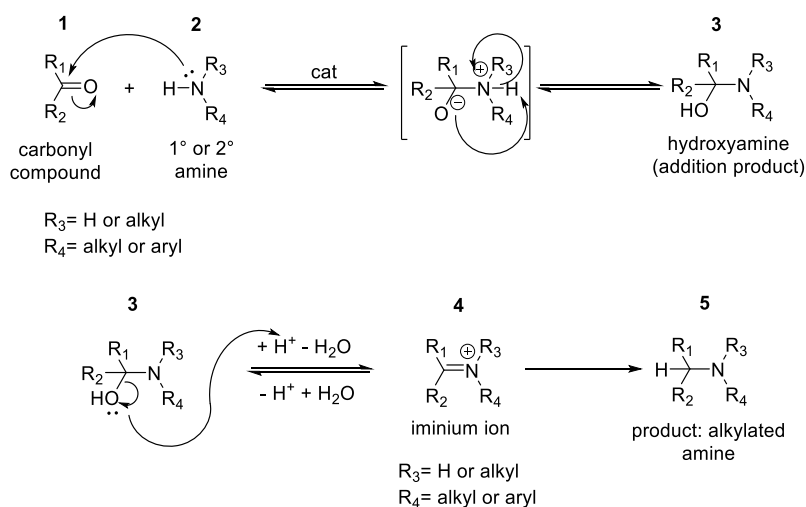


Fig. 13: general reaction pathway and intermediates for a reductive amination reaction.

The reaction pathway involves the initial formation of the intermediate carbinol amine **3** through addition of the amine to the electron-withdrawing carbonyl carbon. **3** then dehydrates to yield an imine. Finally, under the reaction conditions, the imine is protonated to form an iminium ion **4**, which subsequently is reduced to the alkylated amine product **5**.³⁵

Reductive amination, on its own, holds a pivotal role in pharmaceutical and medicinal chemistry due to its advantages and the widespread occurrence of amines in pharmaceutically active compounds.⁴² It is an important transformation when the formation of C-N bonds are required, and recent studies show that at least a quarter of these transformations are performed through reductive amination in the pharmaceutical industry.⁴³ The choice of the reducing agent is critical to the success of the reaction, since it must efficiently reduce the imines (or iminium ions), selectively over aldehydes or ketones under the reaction conditions. The most commonly used direct reductive amination methods can be divided in two classes, that differ from each other depending on the reducing agent.³⁵ The first involves catalytic hydrogenation using molecular hydrogen with

supported metals such as Pt, Pd, Rh or Ni. However, the reaction may yield a mixture of products and low selectivity depending on the chosen reactants.³⁵ The second strategy utilizes hydride reducing agents, particularly sodium cyanoborohydride (NaBH_3CN) for reduction. At pH 3-4 NaBH_3CN reduces aldehydes and ketones effectively, but its reaction becomes very slow at higher pH values. Although selectivity can be easily controlled through pH, the use of this conventional reactant has some limitations: it may require up to a fivefold excess of amine, it is usually slow with aromatic ketones and weakly basic amines, and it can contaminate the final product with cyanide. Additionally, it poses a safety hazard due to its high toxicity and the production of hydrogen cyanide (HCN) and sodium cyanide (NaCN) during the workup process.³⁵

Alternatives to these options are: sodium triacetoxyborohydride [$\text{NaBH}(\text{OAc})_3$]³⁵ (a safer alternative to NaBH_3CN), NaBH_4 , and catalytic transfer hydrogenation (CTH).³⁴

Hydrogenation via Catalytic Transfer Hydrogenation (CTH) represents an intriguing category of catalytic reactions that can exhibit environmentally friendly characteristics. Unlike molecular hydrogen, which poses safety risks due to its flammability and explosiveness, CTH circumvents these issues. Instead of molecular hydrogen, it relies on a hydrogen donor molecule, typically any organic or inorganic species with a sufficiently low oxidation potential to facilitate hydrogen extraction by an active metal catalyst.

Common hydrogen donors include organic compounds like primary and secondary alcohols, hydrocarbons, and cyclic ethers, as well as inorganic substances like hydrazine and phosphonic acid. Secondary alcohols are often preferred as hydrogen donors because they possess lower oxidation potentials compared to primary alcohols. Additionally, they yield ketones, whereas primary alcohols tend to produce aldehydes that may undergo decarboxylation under the reaction conditions. Secondary alcohols can also easily be used as solvents, minimizing the major problem of these transformations, namely the co-production of their oxidated counterparts (ketones) which can be considered as waste and could interfere with the reaction pathway. Utilizing hydrogen donors as solvents inherently diminishes the relative concentration ratio between these donors and the co-produced ketones.

While CTH can be a very useful and green technique,⁴⁴ employing it in a tandem reaction, as done in the current study, would be challenging due to the simultaneous generation of oxidized derivatives of the hydrogen donor.

Regarding the amines used in this project, acetonitrile (ACN) was selected as the precursor, and the corresponding amines were generated in situ within the reaction medium under hydrogen pressure.

Albeit being classified as a class 2 solvent⁴⁵ because of its toxicity (LD50 = 617 mg/kg)⁴⁶ together its rapid adsorption in the organism⁴⁷, it is also true that ACN is produced mainly as a byproduct of the Sohio process for the synthesis of acrylonitrile^{48, 49} and only a small fraction of producers recovers ACN, it is usually burned instead, with polluting emissions of NO_x.⁴² ACN can be used as a useful reactant in the proposed reductive amination process, as its reduction by H₂ under optimized conditions, yields ethyl amine, which can take part in the addition reaction with a carboxyl compound.

It is worth to mention that the reactions pathway and products of the reduction of ACN is intricated, since transamination reactions between the yielded amines and imines happen accordingly to the reaction pathway depicted in Fig. 14. The selectivity between primary, secondary or tertiary amines is primarily determined by the nature of the chosen metal catalyst. The support can also play a major role in steering the selectivity, especially when acid sites are present, such as in the case of silico-aluminates.⁵⁰

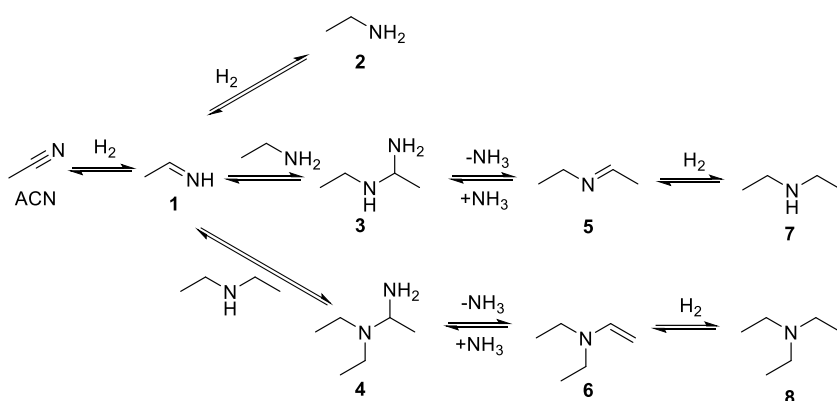


Fig. 14: reaction pathway of the reduction of ACN; **1:** ethanimine; **2:** ethyl amine; **3:** N-ethyl ethanimine; **4:** N-diethyl ethanimine; **5:** ethylethanamine; **6:** diethylethanamine; **7:** diethylamine; **8:** triethylamine.⁵⁰

In summary, ACN was chosen for this project because it can serve as a solvent in the initial stage of the reaction pathway (the oxidation of BnOH to benzaldehyde), where it also plays a role in controlling selectivity. Additionally, it can serve as both reactant and solvent in the subsequent reductive amination of benzaldehyde, facilitating the production of primary, secondary, and tertiary amines.

For this purpose, this study examined nanoparticles of Palladium, Ruthenium, and Rhodium. The most promising outcomes were obtained using Rhodium-supported nanoparticles on *N*-doped carbons derived from chitin for the reductive amination step, which involved ACN, H₂, and Benzaldehyde. Moreover, various metal loadings were explored, ranging from 1 wt% to 5% for both Molybdenum and Rhodium, as well as the formation of their bimetallic counterparts.

1.3. Green Metrics

Since the 1990s, Green Chemistry has supplanted the conventional 'command and control' approach to environmental protection. It has emerged as a superb framework for guiding industrial practices that not only meet regulatory requirements but do so in a profitable manner.⁵¹

Green Chemistry is guided by a set of 12 principles, as detailed in Table 3, that aid in the elimination of hazardous substance use or generation during the design and synthesis of chemical products.

Table 3: *The 12 principles of Green Chemistry*¹

-
1. It is better to prevent waste than to treat or clean up waste after it is formed
 2. Synthetic methods should be designed to maximize the incorporation of all materials used into the final product
 3. Wherever practicable, synthetic methodologies should be designed to use and generate substances that possess little or no toxicity to human health and the environment
 4. Chemical products should be designed to preserve efficacy of function while reducing toxicity
 5. The use of auxiliary substances (e.g. solvents, separation agents, etc.) should be made unnecessary wherever possible and, innocuous when used
 6. Energy requirements should be recognized for their environmental and economic impacts and should be minimized. Synthetic methods should be conducted at ambient temperature and pressure
 7. A raw material or feedstock should be renewable rather than depleting wherever technically and economically practicable
 8. Unnecessary derivatization (blocking group, protection/deprotection, temporary modification of physical/chemical processes) should be avoided whenever possible
 9. Catalytic reagents (as selective as possible) are superior to stoichiometric reagents
 10. Chemical products should be designed to preserve efficacy of function while reducing toxicity
 11. Analytical methodologies need to be developed to allow for real-time, in-process monitoring and control prior to the formation of hazardous substances
 12. Substances and the form of a substance used in a chemical process should be chosen to minimize the potential for chemical accidents, including releases, explosions and fires
-

As these principles started being implemented in chemical reactions, new criteria were devised to quantify the 'greenness' of these processes. This is essential because in order to evaluate the efficiency of a reaction, a means to gauge its success is necessary. Traditional metrics in the field of green chemistry include Atom Economy (AE), E-factor (E), Carbon Efficiency (CE), Stoichiometric Factor (SF), and others, which have been condensed in groups^{51, 52} since they can be disorienting

when applied in large numbers. In this context, a unified metrics toolkit has recently been introduced to assess the sustainability of the protocols. This toolkit analyzes both quantitative and qualitative criteria, encompassing aspects both upstream and downstream of the reactions themselves. Such toolkit has been developed through the CHEM21 project (Chemical Manufacturing Methods for the 21st Century Pharmaceutical Industries) and uses key parameters (shown in Fig. 15, A) to assign values based on a scored system divided in 4 stages: Zero to Third Pass (Fig. 15, B).

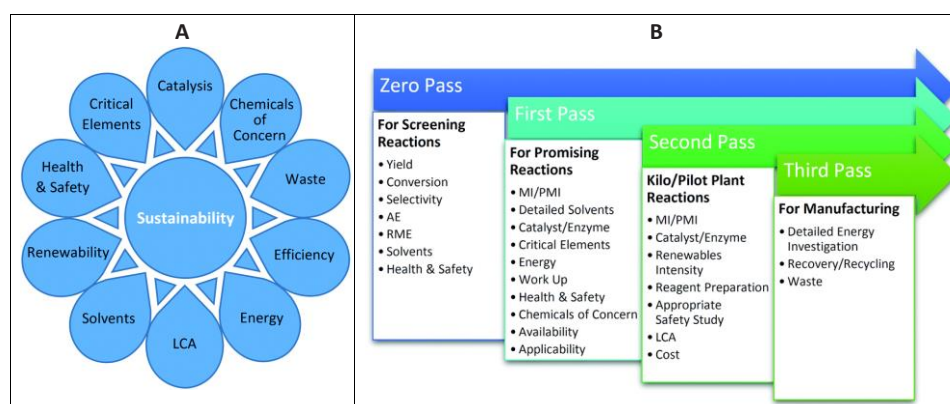


Fig. 15: A) summary of key parameters comprised in the metrics toolkit; B) Structure of the metrics toolkit showing the parameters covered at each Pass.⁵¹

As it is shown in Fig. 15 (B), Zero and First Pass are the most crucial sections for a newly developed process, thus their successful implementation was a primary objective in this work. Second and Third Pass would be considered in the event of scaling up the reaction to pilot scale and beyond.⁵¹ Zero Pass Metric Toolkit was developed for reactions at the discovery level carried out on a small, laboratory scale. The most promising reactions, as indicated by the applied metric, have the potential to advance to the First Pass. Zero Pass is concentrated on identifying issues surrounding the employment of hazardous substances and process efficiency. The factors and metrics in this Pass include yield, conversion and selectivity, Atom Economy (AE), Reaction Mass Efficiency (RME), solvents used, health and safety. Their labelling will be described in the tables below (Tables 4, and 5), and their formulas will be reported (Table 6).

Table 4: Color-code indication system for yield and selectivity in Zero Pass toolkit.⁵¹

Metric	Green flag	Amber flag	Red flag
Yield	>89%	70-89%	<70%

Selectivity	>89%	70-89%	<70%
--------------------	------	--------	------

Table 5: CHEM21 solvent selection guide.⁵¹

Recommended	Water, EtOH, <i>i</i> -PrOH, <i>n</i> -BuOH, EtOAc, <i>i</i> -PrOAc, <i>n</i> -BuOAc, anisole, sulfolane.
Recommended or problematic?	MeOH, <i>t</i> -BuOH, benzyl alcohol, ethylene glycol, acetone, MEK, MIBK, cyclohexanone, MeOAc, AcOH, Ac ₂ O.
Problematic	Me-THF, heptane, Me-cyclohexane, toluene, xylenes, chlorobenzene, acetonitrile, DMPU, DMSO.
Problematic or hazardous?	MTBE, THF, cyclohexane, DCM, formic acid, pyridine.
Hazardous	Diisopropyl ether, 1,4-dioxane, DME, pentane, hexane, DMF, DMAc, NMP, methoxy-ethanol, TEA.
Highly hazardous	Diethyl ether, benzene, chloroform, CCl ₄ , DCE, nitromethane.

Table 6: formulas for the described green metrics parameters of the First Pass of the toolkit.⁵¹

$$\text{Percentage yield} = \frac{\text{moles of product}}{\text{moles of limiting reactant}} \times 100$$

$$\text{Percentage conversion} = 100 - \left(\frac{\text{final mass of limiting reactant}}{\text{initial mass of limiting reactant}} \times 100 \right)$$

$$\text{Percentage selectivity} = \frac{\% \text{yield}}{\% \text{conversion}} \times 100$$

$$\text{AE} = \frac{\text{molecular weight of products}}{\text{total molecular weight of reactants}} \times 100$$

$$\text{RME} = \frac{\text{mass of isolated product}}{\text{total mass of reactants}} \times 100$$

$$\text{OE (optimum efficiency)} = \frac{\text{RME}}{\text{AE}} \times 100$$

$$\text{MI (Mass Intensity)} = \frac{\text{total mass in a process step}}{\text{mass of product}}$$

2. Experimental part

2.1. Materials and equipment:

Benzyl alcohol, furfuryl alcohol, 1,5-bis(hydroxymethyl)furan, 1-phenylethanol, vanillyl alcohol, 1-pentanol, cyclopentanol, acetonitrile, 2-propanol, chitin, EDTA, $\text{CoCl}_2 \cdot 6\text{H}_2\text{O}$, $\text{Fe}(\text{NO}_3)_3 \cdot 9\text{H}_2\text{O}$, $\text{Ni}(\text{Ac})_2 \cdot 4\text{H}_2\text{O}$, $(\text{NH}_4)\text{MoO}_4$, $\text{Pd}(\text{OAc})_2$, $\text{RuCl}_3 \cdot \text{H}_2\text{O}$ and $\text{RhCl}_3 \cdot \text{H}_2\text{O}$ were commercially available compounds sourced from Sigma-Aldrich. If not otherwise specified, reagents and solvents were employed without further purification. Air gas was purchased from SIAD, Italy. Extruding techniques were carried on using a mini-extruder (ZE 12 HMI extruder from Three Tec., Seon, Switzerland)

GC-MS (EI, 70 eV) analyses were performed on a HP5-MS capillary column (L = 30 m, \varnothing = 0.32 mm, film = 0.25 mm). GC (flame ionization detector; FID) analyses were performed with an Elite-624 capillary column (L=30 m, \varnothing =0.32 mm, film=1.8 mm). ^1H , ^{13}C NMR spectra were recorded in the Bruker Advance III HD 400 WB equipped with a 4 mm CP/MAS probe, at 400 and 101 MHz, respectively. Chemical shifts were reported downfield from tetramethylsilane (TMS) and MeOD, $\text{DMSO}-d_6$ and CDCl_3 were used as solvents.

2.2. Synthesis of supported metal nanoparticles on chitin derived N-doped materials

In a typical synthesis, the salt chosen as a metal precursor was dissolved in 2-propanol (60 mL), together with EDTA (1 g) (See Figure 16). EDTA was utilized as a powerful metal complexing agent aimed at achieving a dispersion of metal nanoparticles as uniform as possible over a N-doped carbonaceous chitin support. 1 mmol of the precursor salt were used if the goal was to yield a 5 wt.% metal loading, thus for different wt.%, the corresponding precursor quantities were employed. Subsequently, chitin (5 g) was added to the mixture, which was kept under stirring for 9 h at 80 °C under reflux. The suspension was filtered and the so-obtained solid was dried at 100 °C overnight and finally, heated at 500 °C (heating rate was 5 °C/min) under N_2 flow (10 mL min^{-1}) for 1 h. The catalytic samples achieved by this procedure were labelled as Ni-N/C, Fe-N/C, Co-N/C, Mo-N/C, Rh-N/C, Pd-N/C, Ru-N/C for the nickel, iron, cobalt, molybdenum, rhodium, palladium, and ruthenium catalysts, respectively. Bimetallic samples were synthesized using Mo and Rh metals, as they exhibited the best catalytic activity during evaluation. The synthesis process for these materials was identical to that of their mono-metallic counterparts.

The resulting materials were ground to powder (particle size <200 μm) and stored in the oven (60 °C, 15 mbar) until further use. The yield of the obtained materials was ca. 25±5%, based on the total weight of chitin and the metal precursor used.

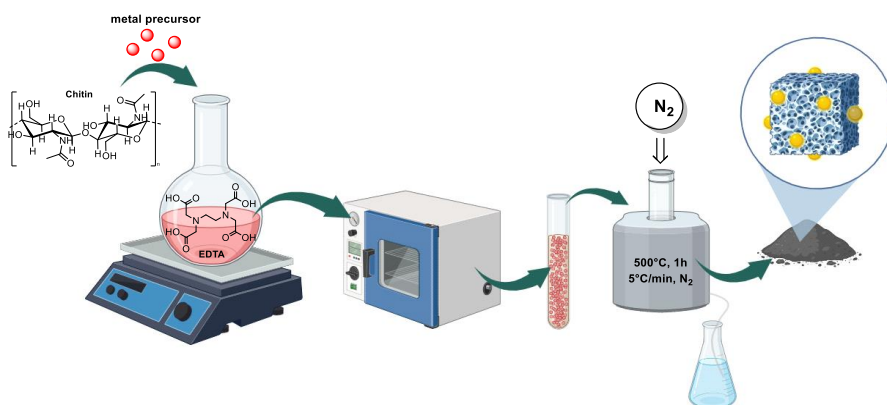


Fig. 16: schematic representation of the synthetic strategy used for the preparation of the catalytic samples.

2.3. Material characterization

Surface chemical composition analysis was conducted using X-ray Photoelectron Spectroscopy (XPS) with a Physical Electronics VersaProbe II Scanning XPS Microprobe. The XPS system was equipped with monochromatic X-ray Al K α radiation and operated at a vacuum level of 10^{-7} Pa. To reference the binding energies, the C 1s peak from adventitious carbon at 284.8 eV was used. High-resolution spectra were obtained with a concentric hemispherical analyzer using a constant energy pass of 29.35 eV and a 200 μ m diameter analysis area. The analysis chamber maintained a pressure below 5×10^{-6} Pa throughout the measurements. Data acquisition and analysis were performed using PHI ACCESS ESCA-F V6 software. A Shirley-type background was subtracted from the signals, and Gauss-Lorentz curves were applied to accurately determine the binding energy of atomic levels for different elements in the recorded spectra.

X-ray powder diffraction (XRPD) patterns were obtained in the laboratory using a PANalytical X'Pert Pro automated diffractometer located in the central research facilities (SCAI) at the University of Málaga. The measurements were performed in the Bragg-Brentano reflection configuration, employing a Ge(111) primary monochromator (Cu K α 1) and the X'Celerator detector. The data acquisition utilized a step size of 0.0167° (2θ). The XRPD patterns were collected within the 4 to 70° range in 2θ , with each step having an equivalent counting time of approximately 60 seconds.

N_2 physisorption measurements were performed using a Micromeritics TriStar 3000 instrument. To prepare the samples, they were subjected to outgassing at 120°C for a duration of 2 h. Subsequently, adsorption and desorption isotherms were recorded at a low temperature of -196°C . Specific

surface areas were determined employing the BET method, while pore volumes were calculated based on the adsorption isotherms. Pore size distributions were estimated utilizing the Barrett, Joyner, and Halenda (BJH) algorithm, which is integrated into the Micromeritics software.

High-Resolution Transmission Electron Microscopy (HRTEM) analysis was conducted using a TALOS F200x instrument operating in STEM mode (Scanning Transmission Electron Microscopy). This instrument was equipped with a High-Angle Annular Dark Field (HAADF) detector and operated at 200 kV with a 200 nA current. Microanalysis was carried out using an Energy-Dispersive X-ray (EDX) Super-X system, which featured four X-ray detectors and an X-FEG beam.

To assess metal leaching, Inductively Coupled Plasma Mass Spectrometry (ICP-MS) was employed, utilizing an Elan DRC-e spectrometer manufactured by PerkinElmer SCIEX.

2.4. Typical oxidation reaction procedure and product analysis

Experiments were conducted within a 50 mL tubular reactor crafted from borosilicate glass (Pyrex). The reactor was charged with benzyl alcohol (1 mmol, 108 mg), along with the catalyst and acetonitrile. The quantities of the catalyst mass and acetonitrile volume were systematically varied during the optimization of reaction parameters. Subsequently, the reactor was positioned inside a jacketed stainless-steel autoclave, which was equipped with a manometer and two needle valves. This autoclave was pressurized to the desired air pressure and heated to the designated temperature. The reaction mixture was maintained under continuous magnetic stirring at a rate of 700 rpm. At the end of the reaction, the autoclave was gradually cooled to room temperature using an ice bath. It was subsequently gently purged. Upon completion of the reaction, a sample of the reaction mixture was withdrawn using a syringe and subjected to analysis by GC-FID to determine reaction conversion and selectivity. Lastly, the samples were evaporated using a rotary evaporator (60°C, 15 mbar). The obtained dried sample was analyzed by GC-MS and NMR in CDCl₃ solvent.

2.5. Typical reductive amination reaction procedure and product analysis

The experiments were conducted within a 50 mL tubular reactor made of borosilicate glass (Pyrex). This reactor was charged with benzaldehyde (1 mmol, 106 mg), along with the catalyst and acetonitrile. The quantities of catalyst mass and acetonitrile volume were systematically varied during the optimization of reaction parameters.

Subsequently, the reactor was placed inside a jacketed stainless-steel autoclave, which was equipped with a manometer and two needle valves. This autoclave was pressurized to the desired

air pressure and heated to the desired temperature. The mixture was continuously stirred magnetically at a rate of 700 rpm. After the completion of the tests, the autoclave was cooled to room temperature using an ice bath, followed by gentle purge. Upon the conclusion of the reaction, a sample of the reaction mixture was withdrawn using a syringe and subjected to GC-FID analysis to determine reaction conversion and selectivity. Lastly, the samples were evaporated using a rotary evaporator (60 °C, 15 mbar). The obtained dried sample was analyzed by GC-MS and NMR in CDCl₃ solvent.

2.6. Typical tandem reaction procedure and product analysis

Experiments were performed in a 50 mL tubular reactor of borosilicate glass (Pyrex) loaded with benzylic alcohol (1 mmol, 108 mg), the catalyst and acetonitrile. The quantity of mass of the catalyst and the volume of acetonitrile used, were studied during the optimization of reaction parameters. The reactor was then placed in a jacketed stainless-steel autoclave equipped with a manometer and two needle valves. The autoclave was pressurized with the desired air pressure and heated to the desired temperature. The mixture was kept under magnetic stirring at a rate of 700 rpm. Upon concluding the first step, the autoclave was allowed to cool to room temperature using an ice bath and was gently purged. Following this, the autoclave was charged with hydrogen at the desired pressure and heated to the optimized temperature for the second stage of the tandem process. After the reaction was completed, an aliquot of the reaction mixture was withdrawn by a syringe and analyzed by GC-FID to determine the reaction conversion and selectivity and rotary evaporated (60 °C, 15 mbar). The obtained dried sample was analyzed by GC-MS and NMR in CDCl₃ solvent. Detailed characterization data can be found in the Appendix Section. The schematic representation of the tandem-reaction pathway is depicted in Fig. 17.

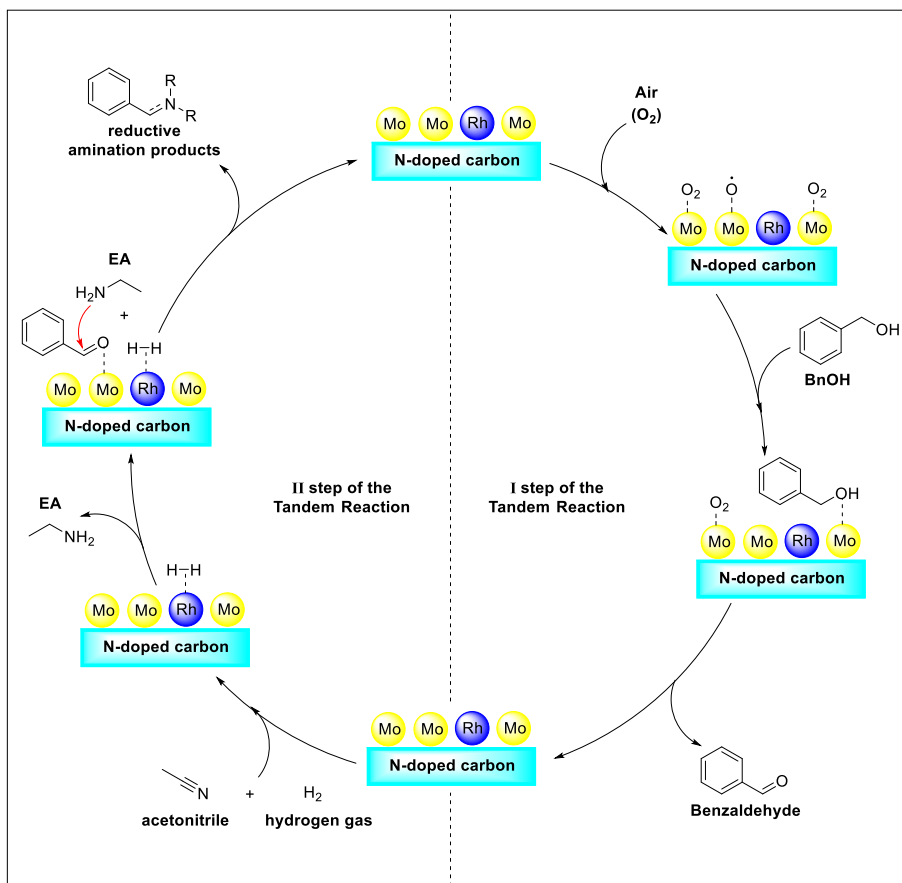


Fig. 17: Schematic representation of the tandem reaction pathway comprising the oxidation of BnOH to benzaldehyde and the reductive amination of the latter.

3. Results and discussion

In this Thesis work, shrimp shell-derived chitin served as a sustainable source of both carbon and nitrogen, eliminating the need for additional nitrogen-containing chemicals such as ammonia or ammonium salts. It's worth noting that our research team has recently demonstrated the effective utilization of chitin and shrimp shell waste for preparing *N*-doped carbons rich in pyridinic nitrogen. Recent computational investigations have provided insights into the chemistry of nitrogen sites and their influence on the metal-support interactions. Among various nitrogen groups, including graphitic and pyrrolic, pyridinic nitrogen sites have proven to be the key contributors for enhancing metal dispersion and preventing leaching. These findings have encouraged us to proceed with the use of *N*-doped carbons derived from chitin as supports for the deposition of metal nanoparticles. The preparation of these *N*-doped carbonaceous materials and their functionalization with metal nanoparticles followed a deposition-precipitation strategy, which could offer advantages in achieving better control over the morphology, size, and dispersion of the synthesized nanoparticles when compared to impregnation methods.

3.1. Characterization of the heterogeneous chitin-supported metal catalysts

The materials obtained, as outlined in the experimental section, underwent a comprehensive characterization using a multitechnique approach, encompassing XRD, N₂-physisorption, XPS, SEM, HRTEM-mapping analyses and ICP-MS.

This section of the thesis will be structured according to the various nanomaterials developed throughout this project. The samples to be discussed here fall into two categories: *mono-metallic catalysts*, including Mo(5%)-N/C, Rh(5%)-N/C, Rh(3%)-N/C, Rh(1%)-N/C; and their corresponding *bi-metallic counterparts*, namely [Rh(5%)-Mo(5%)]-N/C and [Rh(3%)-Mo(5%)]-N/C.

3.1.1. Mono-metallic catalysts:

For simplicity, this section will primarily concentrate on the molybdenum-based and rhodium-based materials, as they displayed higher activity and served as the main catalysts in this work for the oxidation and reductive amination reactions, respectively. Nonetheless, the characterization results of other materials prepared using the same synthetic protocol, such as Ni, Fe, and Co-based catalysts, which exhibited reduced activity in the oxidation reaction, and Pd and Ru-modified samples, also assessed in the reductive amination with lower selectivities, are additionally presented in the appendix section.

Mo(5%)-N/C: The Mo-N/C sample, comprising molybdenum nanoparticles supported on *N*-doped carbons, was synthesized using 1 mmol of ((NH₄)MoO₄) precursor to achieve a final Mo loading of 5

wt.%. Figure 18 below presents the characterization results for this sample, including N_2 -physisorption, XRD and XPS analyses.

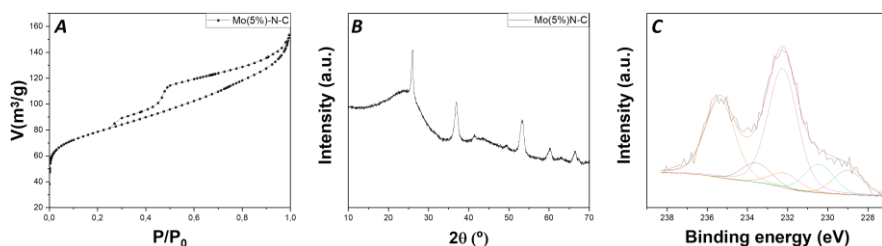


Fig. 18: Characterization of Mo(5%)-N-C sample through **A:** N_2 -physisorption, **B:** XRD and **C:** XPS.

XRD: The crystal structure and arrangement of the synthesized sample were analyzed using XRD. In the XRD pattern of the Mo-N/C sample (as well as for the Ni, Co, and Fe samples, as shown in the XRD diffractograms in the appendix), a distinct peak at approximately 25° was observed. This peak was attributed to the (002) crystallographic plane, related to the parallel stacking of graphene-like sheets. Moreover, a weak peak was also detected at 43° which can be attributed to the (100) crystallographic plane of graphitic carbon arranged in a honeycomb network. The broad shape of this peak was primarily associated with the amorphous nature of the synthesized samples. The observed low crystallinity of the samples was attributed mainly to two factors: i) the thermal protocol employed and ii) the N-doping in the carbonaceous structure, which introduced defect sites. As previously documented in the literature, amorphous materials offer several advantages in terms of catalytic activity compared to their crystalline counterparts, likely due to the greater structural flexibility. The XRD diffractogram of the Mo-based system showed the additional occurrence of well-defined signals around 26° , 35° , 39° , 51° , 59° and 66° . The higher intensity of the peaks at ca. 26° , 35° and 51° , most likely indicated the presence of MoO_2 species along with a minor contribution of MoO_3 , as suggested from the bands at 39° , 59° , and 66° . These findings were indicative of the coexistence of various molybdenum species in the sample.

N_2 -physisorption: The textural properties of the samples were examined through N_2 -physisorption analysis. The observed isotherm exhibited a Type IV pattern, and the adsorption hysteresis was classified as Type II, indicating the formation of mesoporous materials and the presence of disordered networks. Detailed textural properties of the catalysts, such as surface area, pore diameter, and pore volume, are presented in Table 7.

Table 7: N_2 -physisorption parameters for the Mo(5%)-N/C sample.

Material Sample	S_{BET} [m^2/g] ^a	D_{BJH} [nm] ^b	V_{BJH} [cm^3/g] ^c
Mo(5%)-N/C	285	2.9	0.2

XPS: The chemical properties and composition of the synthesized materials were assessed through XPS analysis. The results, depicted in Figure 18, confirmed the presence of metal entities incorporated onto the surface of the N-doped carbonaceous supports.

Mo 3d XPS region of the Mo-N/C sample, was deconvoluted into multiple contributions, at 229.0, 230.4, 232.3, 232.4, 233.5, and 235.3 eV. In particular, the signals at binding energies of 229.0 and 232.4 eV have been previously attributed in the literature to $\text{Mo}\delta^+$ ($0 < \delta < 4$) entities in molybdenum nitride, suggesting the formation of Mo-N bonds. Additionally, the peaks at 230.4 and 233.5 eV were associated with Mo $3d_{5/2}$ and Mo $3d_{3/2}$ contributions of Mo(IV) entities in MoO_2 , while the signals at 232.3 and 235.3 eV were assigned to Mo $3d_{5/2}$ and Mo $3d_{3/2}$ contributions of Mo(VI) entities in MoO_3 . These results, for the most part, supported the findings from XRD analyses. However, a disparity emerged between the two techniques: the XPS spectrum indicated a higher content of MoO_3 on the material surface than that detected by XRD, whereas XRD suggested a higher content of MoO_2 in the bulk sample compared to what was observed by XPS. Furthermore, for Mo(5%)-N/C, the characterization analyses were consistent with the formation of core-shell architectures, wherein a core primarily composed of MoO_2 was enveloped by MoO_3 , with a minor presence of Mo-N groups. XPS analysis of the C 1s, N 1s, and O 1s regions of the Mo(5%)-N/C sample is presented below in Figure 19.

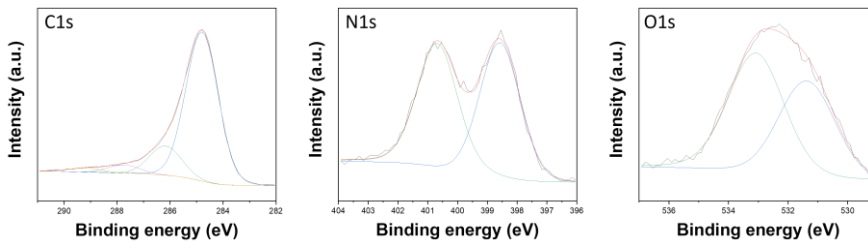


Fig. 19: XPS spectra of C 1s, N 1s, and O 1s regions of the Mo(5%)-N/C sample.

The high-resolution C 1s spectrum of the Mo-N/C sample was deconvoluted into four distinct

contributions located at approximately 284.7, 286.3, 287.8, and 289.3 eV, corresponding to C-C/C=C bonds (graphitic and aromatic carbon), C-OH bonds, C-N/C-O bonds, and C=O bonds, respectively. Furthermore, the N 1s core level spectrum exhibited the presence of two primary contributions at around 398.6 and 400.8 eV, attributed to pyridinic and pyrrolic groups, respectively. Lastly, the O 1s XPS region of the prepared materials revealed two contributions at 531.4 and 533.1 eV, associated with lattice oxygen in metal oxides and adsorbed/bonded water, respectively.

HRTEM images are displayed in Fig. 20. The presence of well-defined laminar structure of the carbonaceous support was noticed, with multiple layers of N-doped carbon stacked on top of each other. High-resolution transmission electron microscopy images confirmed the presence of uniformly distributed molybdenum nanoparticles with an average diameter of (31 ± 2) nm. Additionally, HRTEM micrographs and mapping analysis provided further evidence of the formation of highly dispersed metallic entities throughout the sample. It should be noted that some metal agglomeration was observed in the Mo(5%)-N/C material, as depicted in Figure 20 ('Mo').

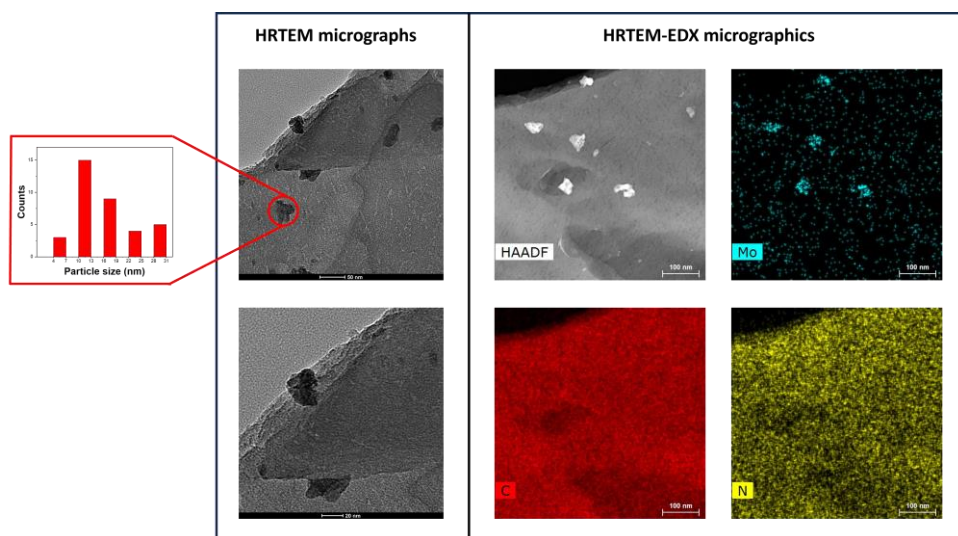


Figure 20: *on the left:* HRTEM micrographs of the Mo(5%)-N/C sample; *on the right:* HRTEM-EDX micrographics of the Mo(5%)-N/C sample.

Rh-N/C: Rhodium nanoparticles supported on N-doped carbons were examined at various loadings, considering the scarcity and cost of rhodium, in order to investigate the relationship between metal loading and catalytic performance in reductive amination reactions. The synthesized and tested

metal loadings included 5 wt.%, 3 wt.%, and 1 wt.%, resulting in the samples being designated as Rh(5%)-N/C, Rh(3%)-N/C, and Rh(1%)-N/C, respectively.

XRD analysis of the rhodium-supported *N*-doped carbonaceous samples was carried out to get insights on their arrangement and crystal structure. The XRD patterns are shown in Fig. 21.

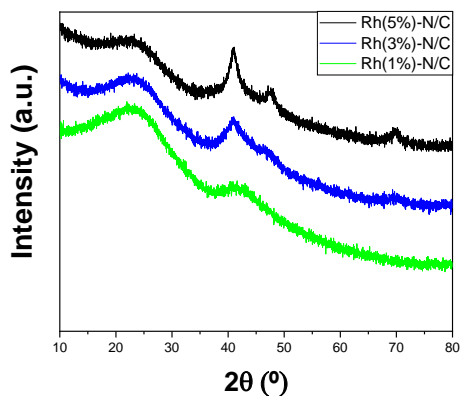


Fig. 21: XRD patterns of the Rh-supported *N*-doped carbonaceous materials with loading of 5wt% (black), 3wt% (blue), and 1wt% (green).

A common feature among all the samples, across various metal loadings, is the presence of a peak at around 25°. This characteristic peak was also observed in the Mo(5%)-N/C sample, as well as in the XRD diffractograms of the Ni, Co, Fe, Ru and Pd samples provided in the appendix. It can be attributed to the presence of the (002) crystallographic plane, which is associated with the parallel stacking of graphene-like sheets. The broad shape of this peak primarily stems from the amorphous nature of the synthesized samples, as already described in the previous section. Furthermore, three weak peaks were identified at 41°, 48°, and 70°, aligning with the typical diffractions associated with the (111), (200), and (220) crystalline planes of metallic Rh. This observation strongly indicates that, during the synthesis process, the Rh³⁺ ions underwent reduction, leading to the formation of metallic Rh, which emerged as the predominant rhodium species within the bulk samples. It is worth noting that the intensity of these three peaks rises with the higher Rh loading, as illustrated in Figure 21, confirming a direct correlation with the metal content.

N₂-pysisorption: The textural properties of the samples were investigated by N₂-pysisorption analysis. As depicted in the figure below (Fig. 22), a comparison is presented between the Rh(5%)-N/C and Rh(1%)-N/C samples, aiming to explore the impact of metal loading on the surface area of

the catalytic material. Both samples exhibited mesoporous characteristics, featuring type-IV isotherms according to the IUPAC classification.

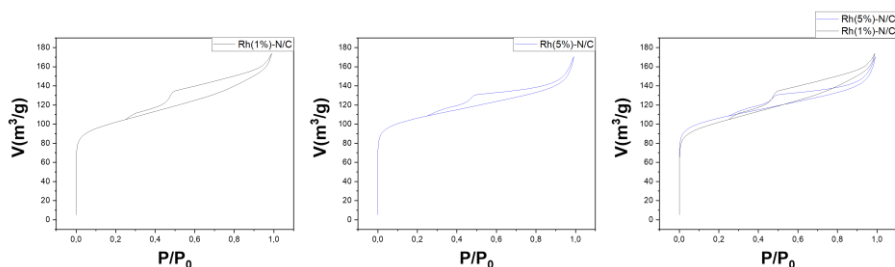


Figure 22: N_2 -physisorption isotherms at -196°C of the prepared Rh metal samples Rh(1%)-N/C, and Rh(5%)-N/C and their comparison.

Table 8 provides information on the BET surface area, mean pore diameter, and pore volume of the prepared Rh-N/C samples. As indicated by these results, minimal differences were observed in terms of surface area when comparing both samples. However, it's noteworthy that they exhibited significantly higher values, nearly 40% greater when compared to molybdenum-based materials. This disparity can likely be attributed to the different metal precursors used in each case. In any case, the slight rise in the mean pore size diameter and the reduction in pore volume of the Rh(5%)-N/C sample when compared to the Rh(1%)-N/C sample likely suggest that the higher metal loading resulted in the occlusion of smaller pores within the carbonaceous matrix.

Table 8: N_2 -physisorption parameters of Rh(1%)-N/C and Rh(5%)-N/C samples.

Material Sample	S_{BET} [m^2/g] ^a	D_{BJH} [nm] ^b	V_{BJH} [cm^3/g] ^c
Rh(1%)-N/C	474	5.8	0.24
Rh(5%)-N/C	489	6.5	0.23

a: S_{BET} : specific surface area was calculated by the Brunauer-Emmett-Teller (BET) equation.

b: D_{BJH} : mean pore size diameter was calculated by the Barret-Joyner-Halenda (BJH) equation.

c: V_{BJH} : pore volumes were calculated by the Barret-Joyner-Halenda (BJH) equation.

XPS: The chemical properties and composition of the synthesized materials were evaluated through XPS analysis. The results are presented in Figures 23, 24, and 25 below, corresponding to the Rh(1%)-N/C, Rh(3%)-N/C, and Rh(5%)-N/C samples, respectively. These results provide confirmation of the

incorporation of metal entities onto the surface of the nitrogen-doped carbonaceous supports.

The C 1s spectra of the Rh samples were deconvoluted into four contributions located at approximately 284.7, 286.1, 287.5, and 289.0 eV. These correspond to C-C/C=C bonds (graphitic and aromatic carbon), C-OH bonds, C-N/C-O bonds, and C=O bonds, respectively. In the O 1s XPS region of the prepared materials, two primary contributions were observed at around 531.1 and 533.1 eV, attributed to lattice oxygen in metal oxides and adsorbed/bonded water, respectively.

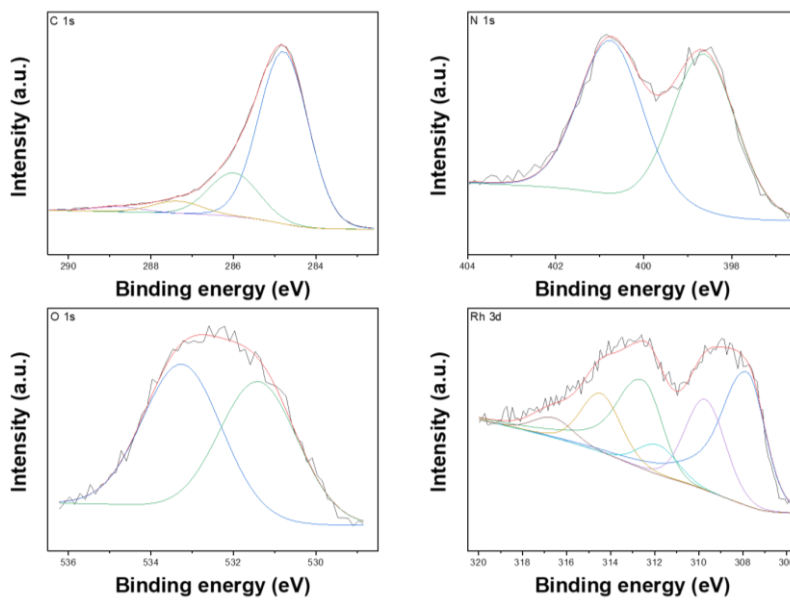


Figure 23: XPS spectra of the Rh(1%)-N/C sample, including C1s, N1s, and O1s and Rh3d regions.

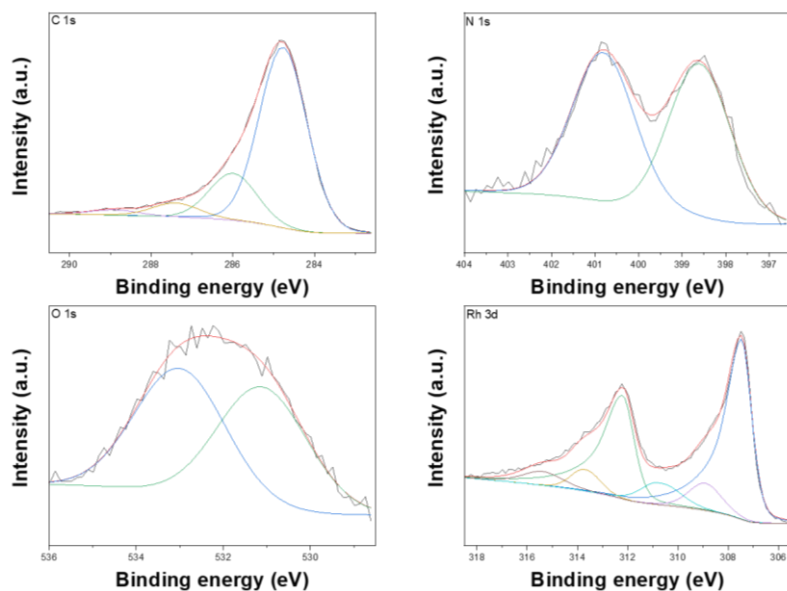


Figure 24: XPS spectra of the *Rh(3%)-N/C* sample, including *C1s*, *N1s*, and *O1s* and *Rh3d* regions.

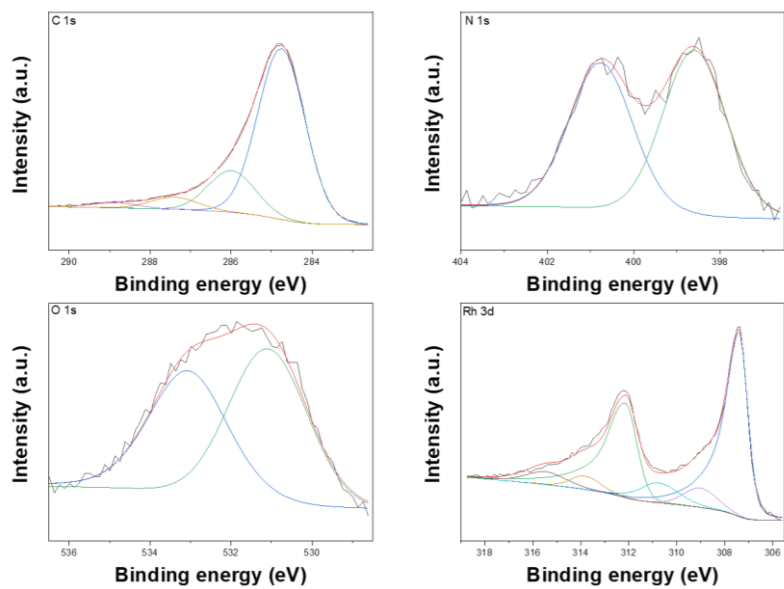


Figure 25: XPS spectra of the *Rh(5%)-N/C* sample, including *C1s*, *N1s*, and *O1s* and *Rh 3d* regions.

In the Rh 3d region, peaks characteristic of both Rh⁰ and Rh³⁺ were detected with respective binding energies of 307 and 309 eV. More specifically, as shown in the Fig. 26, the peaks at 307 and 312 eV are assigned specifically to Rh 3d_{5/2} and Rh 3d_{3/2}, distinctive of Rh⁰, and the peaks at 309 and 314 eV are respectively assigned to Rh 3d_{5/2} and Rh 3d_{3/2}, distinctive of Rh³⁺. Furthermore, the presence of additional contributions at around 310.7 and 315.4 eV strongly indicates the formation of Rh-N bonds. This formation is likely to enhance the stability of the samples, thereby preventing any leaching during the catalytic transformations.

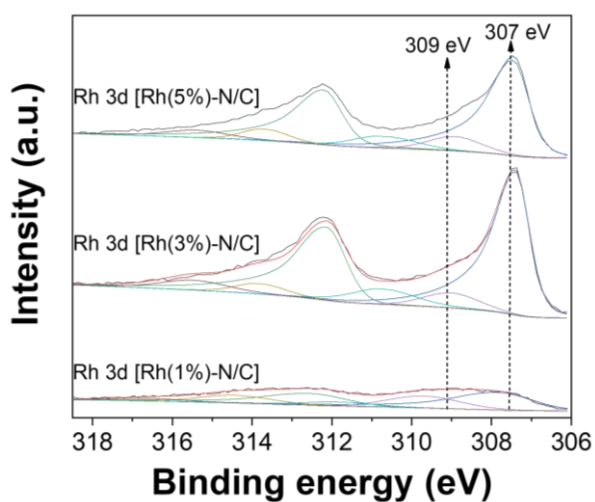


Figure 26: Rh3d regions of the Rh samples Rh(1%)-N/C, Rh(3%)-N/C, and Rh(5%)-N/C.

Regarding the XPS spectra of the N1s regions in both samples, the core-level spectrum revealed the presence of two main peaks at ca. 398.6 and 400.8 eV, associated to pyridinic (N_p) and pyrrolic (N_{pyr}) groups, respectively. These results are depicted in Fig. 27. An intriguing observation worth noting in this case is a slight decrease in pyridinic nitrogen content as the rhodium content in the samples increases. This phenomenon is most likely attributed to the increasing formation of nitrogen-metal bonds, which consequently leads to a reduction in the presence of pyridinic nitrogen on the surface.

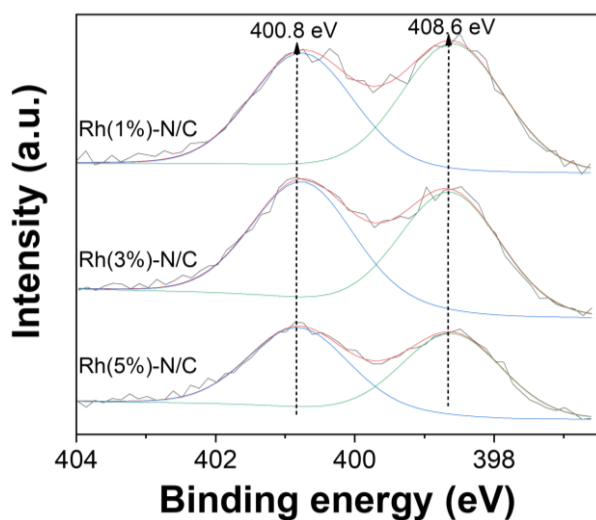


Figure 27: *N1s* regions of the Rh samples Rh(1%)-N/C, Rh(3%)-N/C, and Rh(5%)-N/C.

3.1.2. Bimetallic catalysts

Bimetallic systems were prepared employing 5 wt.% molybdenum loading and either 3 wt.% or 5 wt.% rhodium loading, labelled as [Rh(3%)-Mo(5%)]-N/C and [Rh(5%)-Mo(5%)]-N/C, respectively.

[Rh(3%)-Mo(5%)]-N/C sample was chosen as the representative bimetallic sample for characterization in this work. It was anticipated that this material would exhibit distinct characteristics compared to its monometallic counterparts, specifically the Mo(5%)-N/C and Rh(3%)-N/C samples. The possibility of interactions between the Rh and Mo metal centers was not ruled out, which could result in unique physicochemical properties and varying catalytic activity in the reactions under investigation. The discussion of these aspects will be presented in the Catalytic Activity section.

XRD: The crystal structure and arrangement of the synthesized sample were analyzed using XRD. In the XRD pattern of the bimetallic [Rh(3%)-Mo(5%)]-N/C sample, as illustrated in Figure 28, the peak at approximately 25° is evident, similar to the previously examined samples. This peak again confirmed the presence of the (002) crystallographic plane, associated with the parallel stacking of graphene-like sheets. The broadness of this peak is attributed to the amorphous nature of the synthesized samples.

Furthermore, three distinct and sharp peaks at 41.0, 47.7, and 69.9° were ascribed to the characteristic diffractions associated with the (111), (200), and (220) crystalline planes of metallic

Rh. These results mirrored those observed for the monometallic counterpart. Nevertheless, notable disparities in signal intensity were discernible, with the bimetallic sample exhibiting more well-defined peaks. Intriguingly, no additional signals related to the presence of molybdenum entities were detected. This observation strongly suggests the formation of well-dispersed low size metal nanoparticles or even clusters. However, confirmation of this phenomenon would require TEM analysis.

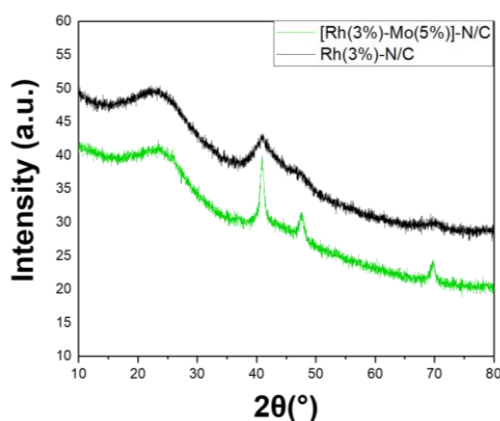


Figure 28: XRD patterns of the sample [Rh(3%)-Mo(5%)]-N/C, with Rh and Mo supported on N-doped carbonaceous materials with loadings of 3wt% and 5wt% respectively (**green**) compared with the monometallic sample Rh(3%)-N/C (**black**).

N₂-physisorption: The textural properties of the bimetallic sample were investigated by N₂-physisorption. As depicted in the figure below (Fig. 29), the isotherm of [Rh(3%)-Mo(5%)]-N/C is presented alongside a comparison with both the Rh(1%)-N/C and Mo(5%)-N/C samples. This analysis aims to ascertain whether the properties of this bimetallic sample differ from those of its monometallic counterparts.

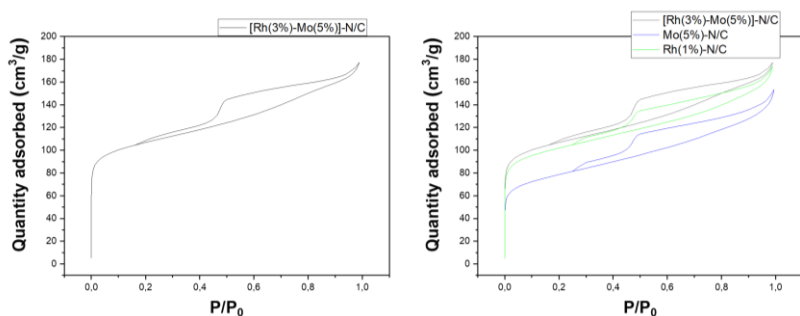


Figure 29: N_2 -physorption isotherms at -196°C of the prepared bimetallic $[\text{Rh}(3\%)\text{-Mo}(5\%)]\text{-N/C}$ sample, and its comparison with the isotherms of the $\text{Rh}(1\%)\text{-N/C}$, and $\text{Mo}(5\%)\text{-N/C}$ samples.

The N_2 -physorption analysis of the $[\text{Rh}(3\%)\text{-Mo}(5\%)]\text{-N/C}$ sample aligns with the characteristics observed in the previously described monometallic materials, exhibiting a type-IV isotherm according to the IUPAC classification, reasonably associated with the presence of mesoporous structures. In the following Table 9, data regarding the BET surface area, the mean pore diameter, and the pore volume of the prepared bimetallic sample are shown, in comparison with those of the $\text{Rh}(1\%)\text{-N/C}$, and $\text{Mo}(5\%)\text{-N/C}$ samples. As indicated in Table 9, the surface area, mean pore diameter, and pore volume of the prepared bimetallic sample closely resembled those obtained for the rhodium monometallic sample. This similarity strongly suggests that the formation of the mesoporous architecture was primarily influenced by the rhodium precursor.

Table 9: N_2 -physorption analysis of $\text{Rh}(1\%)\text{-N/C}$ and $\text{Rh}(5\%)\text{-N/C}$ samples.

Material Sample	S_{BET} [m^2/g] ^a	D_{BJH} [nm] ^b	V_{BJH} [cm^3/g] ^c
$[\text{Rh}(3\%)\text{-Mo}(5\%)]\text{-N/C}$	496	5.4	0.25
$\text{Rh}(1\%)\text{-N/C}$	474	5.8	0.24
$\text{Mo}(5\%)\text{-N/C}$	285	2.9	0.20

a: S_{BET} : specific surface area was calculated by the Brunauer-Emmett-Teller (BET) equation.

b: D_{BJH} : mean pore size diameter was calculated by the Barret-Joyner-Halenda (BJH) equation.

c: V_{BJH} : pore volumes were calculated by the Barret-Joyner-Halenda (BJH) equation.

XPS: The chemical properties and composition of the synthesized bimetallic material were evaluated through XPS analysis. The results are shown below in the Fig. 30.

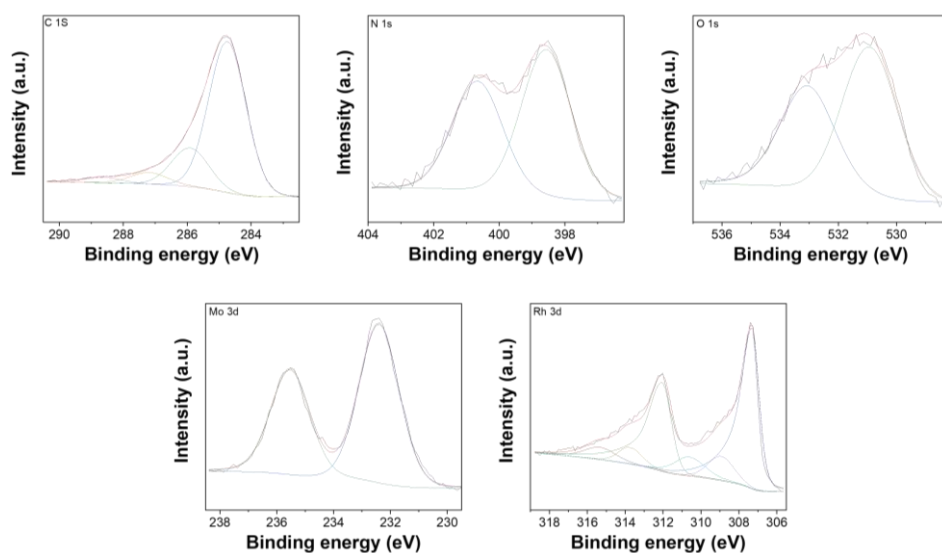


Figure 30: XPS spectra of the *[Rh(3%)-Mo(5%)]-N/C* sample, including C 1s, N 1s, and O 1s, Rh 3d, and Mo 3d regions.

The C 1s spectra of the bimetallic sample, analogously to the other prepared materials previously discussed, shows four distinct contributions located at ca. 284.7, 285.9, 287.3, and 288.8 eV, corresponding to C-C/C=C bonds (graphitic N_g and aromatic carbon), C-OH bonds, C-N/C-O bonds, and C=O bonds, respectively. In addition, the N 1s regions of the sample, equally to the monometallic samples, showed the presence of two main peaks at ca. 398.6 and 400.8 eV, due to pyridinic (N_p) and pyrrolic (N_{pyr}) groups, respectively. Moreover, in the O 1s XPS region of the bimetallic sample two main contributions were displayed at approximately 531.0 and 533.1 eV, associated with lattice oxygen in metal oxides and adsorbed/bonded water, respectively. This confirms that the XPS spectra of the C 1s, N 1s, and O 1s regions align with those of the monometallic materials.

Moving forward, we examined the Mo 3d and Rh 3d regions (Fig. 30). In the Mo 3d XPS region of the Mo-N/C sample, two distinct contributions were identified, in contrast to the monometallic Mo(5%)-N/C, which exhibited six contributions. The two observed peaks were situated at 232.4 and 235.5 eV, indicative of MoO_3 . Notably, the signals at binding energies of 230.4 and 233.5 eV, associated with Mo $3d_{5/2}$ and Mo $3d_{3/2}$ contributions of Mo(IV) in MoO_2 , previously observed in the monometallic material, were absent in the bimetallic sample. No signals related to Mo-N bonds

were detected in the Mo 3d spectrum of the bimetallic sample. This observation is likely attributed to a stronger affinity between rhodium and nitrogen, which results in the formation of Rh-N bonds instead of Mo-N bonds. The disparities between the XPS spectra in the Mo 3d regions of the bimetallic and monometallic samples are depicted in Figure 31.

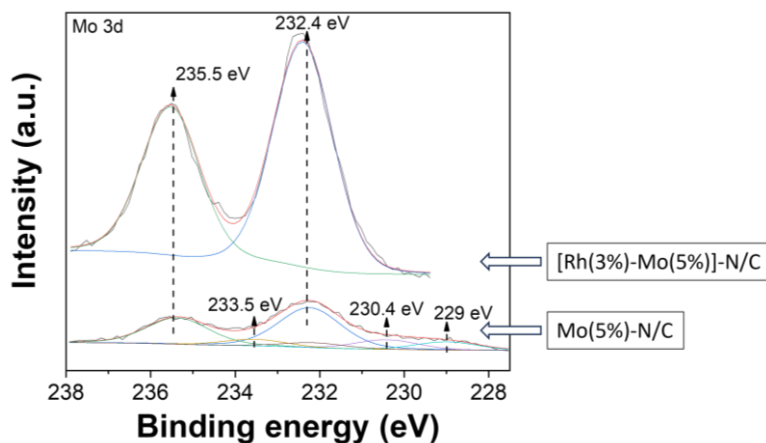


Figure 31: Mo 3d regions of the [Rh(3%)-Mo(5%)]-N/C, and Mo(5%)-N/C samples.

In turn, within the Rh 3d regions of the XPS spectrum (illustrated in Fig. 32), we observed identical signals to those previously discussed in the Rh 3d region of the monometallic Rh(3%) sample (as shown in Fig. 35). This observation suggests that the presence of molybdenum did not influence the chemical nature of the rhodium entities.

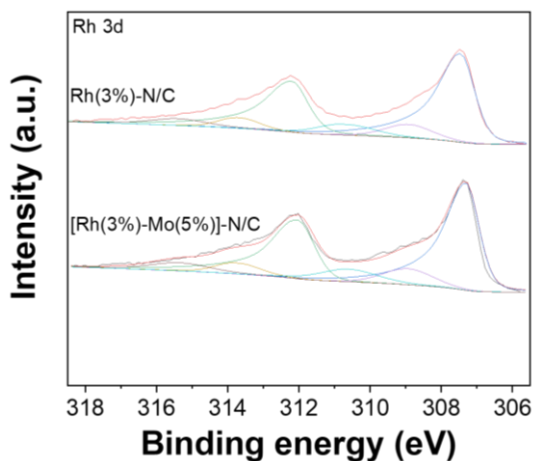


Figure 35: Rh 3d regions of the [Rh(3%)-Mo(5%)]-N/C, and Rh(3%)-N/C samples.

3.2. Catalytic activity

To assess the catalytic performance of the synthesized nanomaterials in this study, a tandem-reaction approach was employed. This approach involves the selective oxidation of an aromatic alcohol to its corresponding aldehyde, followed by the reductive amination of the aldehyde to produce the desired aminated products. The selection of the appropriate protocol and reaction conditions was crucial to optimize the selectivity of both reaction steps, ultimately leading to the highest possible yield of the final aminated product.

Benzyl alcohol (BnOH) was selected as model substrate for the oxidation reaction, resulting in the formation of benzaldehyde. Subsequently, benzaldehyde was utilized as substrate for the consecutive reductive amination reaction, leading to the production of amines and imines.

The subsequent sections of this thesis will delve into a comprehensive discussion of the outcomes obtained while optimizing the reaction conditions for the above-mentioned process. This discussion will be organized into distinct segments, starting with the oxidation reaction of BnOH, followed by the reductive amination of benzaldehyde. Additionally, we will explore the tandem reaction encompassing both steps, the suitability of the optimized protocols for different substrates, the recyclability and reusability of the catalytic materials, and lastly, an assessment of a mechanochemical approach within this synthesis.

3.2.1. Selective oxidation reaction of BnOH towards Benzaldehyde using air as oxidant agent.

Benzyl alcohol was oxidized using air as a green oxidant agent, selected for both safety and economic reasons. Batch experiments were carried out in autoclaves (stainless-steel pressurized vessels) in which a mixture of BnOH (1 mmol, 108 mg) and the investigated catalyst (the samples are reported in the Table 10) in varying quantities (ranging from 25 to 100 mg) was allowed to react under different conditions, including a range of temperatures (from 130 to 170 °C), pressures (from 1 to 20 atm), times (from 4 to 24 h), and solvent volumes (ACN, from 6 to 10 mL). The results obtained were corroborated by NMR and GC/MS analyses of the products.

To gain a deeper understanding of the impact of the catalytic nanomaterials, we conducted additional control experiments without the use of any catalyst. These experiments revealed that, under the conditions specified in Table 10 (excluding the catalyst), the highest yield of benzaldehyde achieved was merely 3%, hence demonstrating the fundamental role of the catalytic system for the progress of the reaction. The schematic reaction pathway of this process is illustrated in Fig. 36.

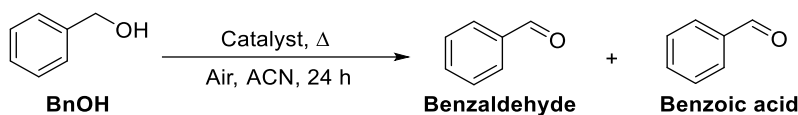


Figure 36: scheme of reaction pathway for the oxidation of BnOH.

To initiate our investigations into this reaction using the heterogeneous Mo-based N-doped catalyst, we conducted a literature review of standard reaction conditions. Additionally, we drew upon previous research conducted by our research group to determine the initial parameters used in our preliminary tests. This set of reaction parameters, as described in a recent publication by our research group (utilizing 1 mL of ACN), yielded impressive results with 91% selectivity and 95% conversion in the production of benzaldehyde. Consequently, these parameters served as the foundation for subsequent investigations. However, in the subsequent stages, we used 10 mL of ACN instead, as it also serves as a reactant in the consecutive reductive amination of benzaldehyde.¹⁷ Further details regarding the impact of the solvent in both reactions, particularly in the reductive amination step, will be expounded upon in the forthcoming sections.

Table 10: Initial reaction parameters for the investigation of the oxidation of BnOH.

Catalyst	Amount of the catalyst mg	T °C	P bar	T h
Mo-N/C	50	130	20	24

Temperature was the initial variable scrutinized during the parameter optimization of the oxidation reaction of BnOH (Figure 37 A). The most favorable outcomes were observed at 170 °C, with both conversion and selectivity exceeding 99%. Conversely, lower temperature values of 130 and 150 °C, although yielding complete selectivity, resulted in reduced conversion values of 52% and 75%, respectively.

The impact of *Pressure* on the reaction outcome was explored by reducing it from 20 bar to ambient pressure (1 atm), while maintaining the temperature at 170 °C, and keeping all other reaction parameters consistent with those specified in Table 10 (Figure 37 B). Notably, both conversion and yield remained consistently above 99% even under standard atmospheric air pressure. This result significantly enhances the safety and cost-efficiency of the system. It is well-known that high pressures represent a safety hazard and economic costs, both in the capital and operating costs of a scalable batch process.⁵³

The impact of *reaction time* was investigated by varying the duration from 24 hours to 4 hours, as depicted in Figure 37C. The results presented in Figure 37 C reveal that at an 18-hour reaction time, quantitative conversion and selectivity were achieved. In contrast, shorter reaction times ranging from 4 to 12 hours consistently yielded conversion values hovering around 45%.

The *solvent volume* was subsequently scrutinized, within a range from 10 mL to 4 mL, and quantitative results were still achieved by using solvent volumes above 6 mL. However, it was later determined that 10 mL of ACN should continue to be employed. This decision was based on the findings of the solvent optimization for the reductive amination step, where the use of 6 mL led to undesirable selectivity. Further comments on this matter will be provided upon in the subsequent section.

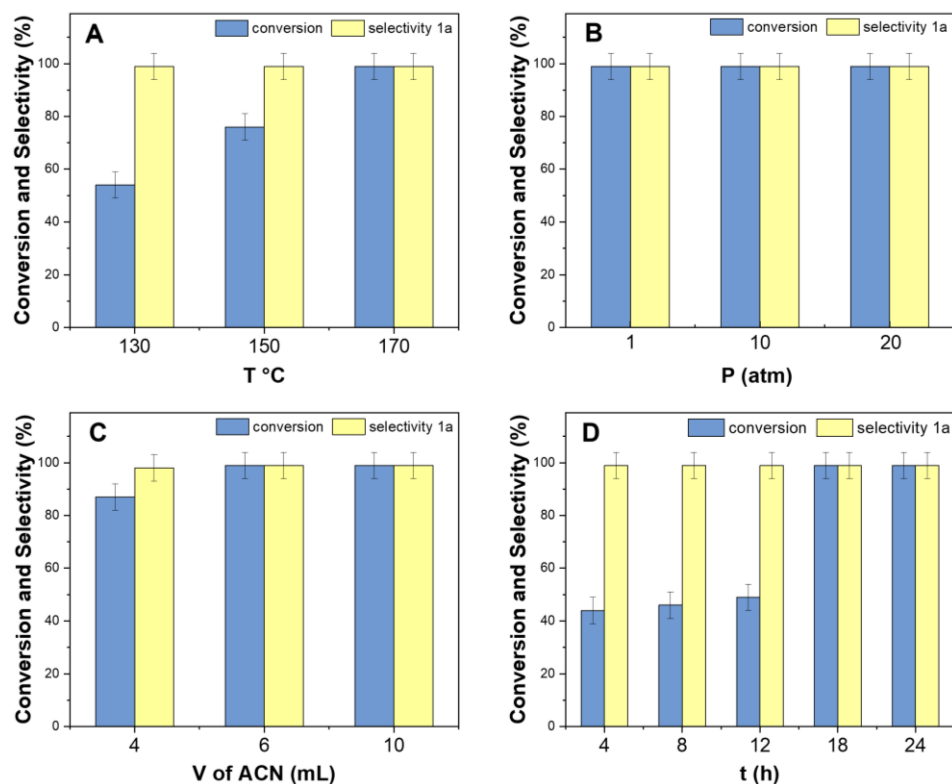


Figure 37: optimization of reaction parameters: **A)** temperature, **B)** pressure, **C)** volume of solvent and **D)** reaction time) of the oxidation reaction of BnOH using the Mo(5%)-N/C catalytic sample.

The catalyst amount was then examined (Figure 38 A), revealing that quantitative conversion and selectivity towards benzaldehyde remained above 99% when using half of the initial mass of the Mo(5%)-N/C sample, specifically 25 mg. All other parameters were set in accordance with the previously optimized conditions, including temperature (170 °C) and pressure (1 atm). It was determined that 25 mg was the optimal catalyst loading, as lower loadings of 10 mg still yielded good results but with slightly lower conversion at around 88%. Conversely, a higher catalyst amount (100 mg) led to reduced benzaldehyde selectivity, accompanied by the formation of benzoic acid. In Figure 38B, we present a study conducted under the optimized reaction conditions, utilizing different catalytic samples, namely Mo(5%)-N/C, Rh(3%)-Mo(5%)-N/C, Rh(5%)-Mo(5%)-N/C, and a mechanical mixture of Mo(5%)-N/C and Rh(5%)-N/C. These tests were conducted to assess the influence of the presence of Rh active sites, which are essential for the second stage of the tandem reaction, during the oxidation reaction of BnOH.

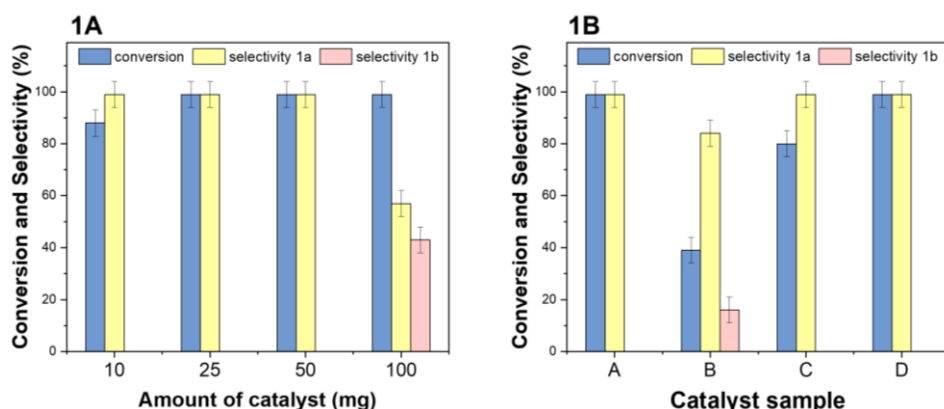


Figure 38: **1A:** * optimization of the amount of chosen the catalyst used [Mo(5%)-N/C]; **1B:** * catalytic tests using different materials: **A:** Mo(5%)-N/C, **B:** [Rh(3%)-Mo(5%)]-N/C, **C:** [Rh(5%)-Mo(5%)-N/C, **D:** mechanical mixture of Mo(5%)-N/C and Rh(5%)-N/C. * The reaction conditions used for these investigations were $T=170\text{ }^{\circ}\text{C}$, $P=1\text{ atm}$, $t=18\text{ h}$, $V\text{ of ACN}=10\text{ mL}$.

The bimetallic catalytic samples were synthesized maintaining the same quantity of molybdenum as in the optimized 25 mg of Mo(5%)-N/C. As explained in the "Materials and Methods" section of this thesis, the catalytic samples were prepared using 1 mmol of the chosen metal precursor on 5 g of chitin, along with 1 g of EDTA as the chelating agent. For the bimetallic materials, Rh(3%)-Mo(5%)-N/C and Rh(5%)-Mo(5%)-N/C, an additional 0.6 mmol and 1 mmol of Rh precursor salt were

respectively incorporated, in addition to the 1 mmol of the Mo precursor salt. When using catalytic materials having both Rh and Mo metals active sites, the mechanical mixture of Mo(5%)-N/C and Rh(5%)-N/C yielded the best results (quantitative conversion and selectivity). Conversely, the bimetallic samples, as synthesized, exhibited reduced conversion values of 39% and 78% for Rh(3%)-Mo(5%)-N/C and Rh(5%)-Mo(5%)-N/C, respectively. This was observed alongside diminished benzaldehyde selectivity, particularly in the case of the Rh(3%)-Mo(5%)-N/C material. These results may be inherently connected to the changes identified in the chemical nature of the molybdenum entities within the bimetallic samples, as indicated by the XPS results.

The herein optimized conditions for the selective oxidation of BnOH to Benzaldehyde are summarized in the following Tab 11, resulting in quantitative conversion and selectivity.

Table 11: *optimized reaction parameters for the selective oxidation of BnOH to benzaldehyde.*

Catalyst	Amount of the catalyst	T	P	T
	mg	°C	atm	h
Mo(5%)-N/C	25	170	1	18

3.2.2. Reductive amination reaction of benzaldehyde.

Benzaldehyde served as the model substrate for conducting reductive amination reactions. Batch experiments were conducted in autoclaves (stainless-steel pressurized vessels). In these experiments, a mixture comprising benzaldehyde (1 mmol, 106 mg) and the investigated catalyst (detailed in subsequent pages) in varying quantities (ranging from 25 to 100 mg) was allowed to react under different conditions, including a range of temperatures (ranging from 60 to 100 °C), hydrogen pressures (ranging from 10 to 50 bar), reaction times (from 4 to 24 hours), and solvent volumes (ACN, from 6 to 10 mL). The obtained results were confirmed through NMR and GC/MS analyses of the products.

Additional blank experiments were conducted in the absence of catalytic materials to assess the impact of the catalyst, and the obtained results yielded only minimal product traces. These experiments were carried out with the parameters outlined in Table 12 (except for the catalyst).

Figure 39 illustrates the scheme of the reaction pathway of this process.

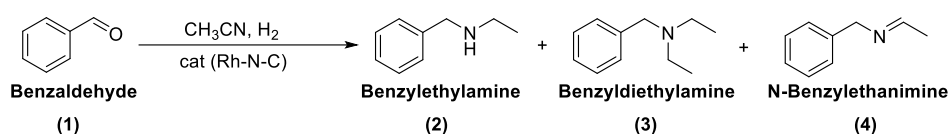


Figure 39: schematized reaction pathway for the reductive amination of benzaldehyde.

To initiate our investigations into this reaction using the heterogeneous Rh-based N-doped catalyst, we conducted a thorough review of standard reaction conditions in the literature. Additionally, we relied on prior research conducted by our research group to establish the initial parameters employed in our preliminary tests. In particular, our research group had previously developed a series of titania-supported Rh catalyst, which were employed in the reductive amination of furfural.⁵⁴

Table 12: starting reaction parameters for the reductive amination of benzaldehyde.

Catalyst	Amount of the catalyst mg	T °C	P _{H₂} bar	t h
Rh-N/C	50	100	30	24

Throughout the parameter optimization for this stage of the tandem reaction, the three primary products observed were represented as (1), (2), and (3) in Figure 39. Other products were obtained with low selectivity and are categorized as "other" in the subsequent discussion. They will be detailed in the Appendix section of this thesis.

Compared to other tested materials, such as palladium and platinum-based catalysts (characterization included in the Appendix section), Rh-based heterogeneous catalysts delivered the most promising results in converting benzaldehyde into reductive amination products.

Pd and Pt catalysts showed good conversion and activity, although selectivity was aimed at the reduction of the substrate rather than the reductive amination.

Nevertheless, it is worth noting that Rh is a noble metal with limited availability and a high, often fluctuating, price.⁵¹ For this reason, the initial focus of the work was on assessing catalytic activity using various Rh metal loadings, including the study of both mono and bimetallic compounds. The exploration of bimetallic compounds had previously been conducted for the oxidation of BnOH, as the ultimate objective was to perform both of these transformations consecutively without the need to change the catalyst in between.

The investigated catalytic samples for the reductive amination of benzaldehyde can be broadly classified into *mono-metallic materials*: Rh(5%)-N/C (5 wt.% loading of Rh), Rh(3%)-N/C (3 wt.% loading of Rh), Rh(1%)-N/C (1 wt.% loading of Rh on the material); *Bi-metallic materials*: [Rh(5%)-Mo(5%)]N/C (5 wt.% loading of Rh and 5 wt.% loading of Mo), [Rh(3%)-Mo(5%)]N/C (3 wt.% loading of Rh and 5 wt.% loading of Mo). Finally the catalytic activity of the *mechanical mixtures* of Rh(5%)-N/C with Mo(5%)-N/C, and Rh(3%)-N/C with Mo(5%)-N/C, respectively, were studied.

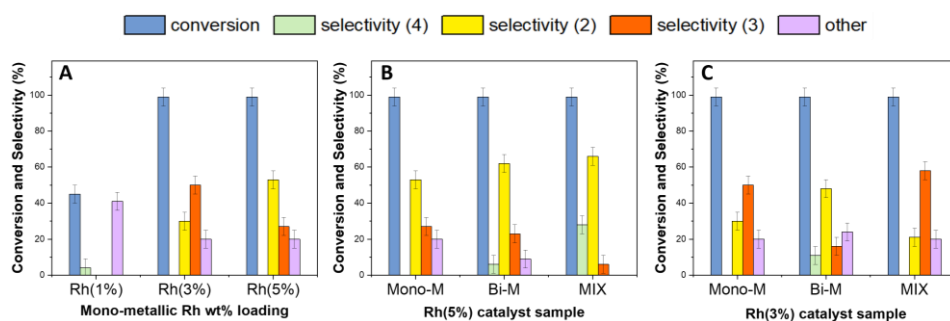


Figure 40: * graphed data on catalysts tests: **A)** study on Rh-metal loading on the material; **B)** compared catalytic activity between Mono-metallic Rh(5wt%), Bi-metallic Rh(5wt%)-Mo(5wt%), and the mixed samples with Rh(5wt%) and Mo(5wt%); **C)** compared catalytic activity between Mono-metallic Rh(3wt%), Bi-metallic Rh(3wt%)-Mo(5wt%), and the mixed samples with Rh(3wt%) and Mo(5wt%).*reaction conditions for all of the tests reported in the following Fig. 40 are shown in Table 12.

The optimization of reaction conditions was conducted after selecting the most promising catalytic materials based on their performance in converting benzaldehyde, while also considering their selectivity towards (1), (2), or (3). In the evaluation of mono-metallic Rh-based catalytic samples, Rh(5%)-N/C and Rh(3%)-N/C demonstrated excellent results, yielding quantitative conversions towards secondary (2) (with 53% selectivity) and tertiary amine (3) (with 55% selectivity), respectively. However, the Rh(1%)-N/C sample exhibited subpar performance, with conversion values hovering around 45%, steering selectivity towards undesired products. Figure 40 presents the results of this analysis. With such results in mind, Rh loadings of 3 wt.% and 5 wt.% were chosen for further investigations. Bimetallic counterparts were synthesized for these loadings (using a 5 wt.% Mo loading) or employed in mechanically made mixtures with the previously analyzed Mo(5%)-N/C sample. The catalytic activity of these combinations is depicted in Figure 40 B) and C) for Rh loadings of 3 wt.% and 5 wt.%, respectively.

In this context, both the bimetallic counterparts and the mechanical mixtures with Mo metal exhibited changes in selectivity. Specifically, the bimetallic [Rh(3%)-Mo(5%)]-N/C sample demonstrated a higher selectivity (48%) for the secondary amine (2) as opposed to the tertiary amine (3) (16% selectivity). Conversely, both the mono-metallic Rh(3%)-N/C and the mechanical mixture between Rh(3%)-N/C and Mo(5%)-N/C yielded the tertiary amine (3) as the predominant product, with selectivity rates of 50% and 58%, respectively. (guarda trietil ammina)

This behavior can be rationalized by considering that Rh(3%)-N/C is inherently less active than the Rh(5%)-N/C sample due to its lower Rh-metal loading. When examining the reduction products of ACN as shown in Figure 14, it becomes evident that ethylamine, the reactant essential for the amination of the aldehyde, is generated using only 2 moles of hydrogen in two consecutive reduction steps. However, if ethylamine is produced rapidly, it can react with the intermediate of this process, which is imine 2 (ethanimine as depicted in Figure 14), formed after the consumption of 1 mole of hydrogen from ACN. This alternative reaction pathway further leads to the formation of triethylamine, which does not participate in the amination of the aldehyde. In summary, the Rh(5%)-N/C sample, owing to its higher activity, results in the production of triethylamine or other products of acetonitrile reduction rather than ethylamine. Consequently, the lower concentration of ethylamine in the reaction medium promotes the more favorable formation of the secondary amine over the tertiary amine. This hypothesis was validated through GC-FID and GC-MS analyses performed on various reaction samples, which detected a higher concentration of triethylamine in the samples catalyzed using Rh(5%)-N/C compared to those with Rh(3%)-N/C.

Conversely, the [Rh(5%)-Mo(5%)]-N/C sample exhibited a preference for the secondary amine (2), with a selectivity of 62%, mirroring the selectivity observed in the mono-metallic and mechanically mixed samples with 5 wt% Rh loadings (53% and 66% selectivity, respectively). Following this preliminary investigation, it was determined that the catalytic sample exhibiting the highest selectivity for the secondary amine (2) was the mechanically mixed combination of Rh(5%)-N/C and Mo(5%)-N/C. Conversely, the catalytic sample displaying the highest selectivity for the tertiary amine (3) was the mechanically mixed combination of Rh(3%)-N/C and Mo(5%)-N/C. Consequently, the mechanically mixed samples demonstrated a comparable yet improved catalytic activity in the reductive amination of benzaldehyde when compared to the monometallic Rh-metal samples.

Furthermore, taking into account the limited catalytic activity observed in the oxidation of BnOH by the bimetallic samples and considering the results of the reductive amination reaction, the mechanical mixtures of Rh(5%)-N/C with Mo(5%)-N/C and Rh(3%)-N/C with Mo(5%)-N/C were

selected for the development of the tandem-reaction process, rather than the synthesized bimetallic counterparts.

The subsequent paragraphs encompass the parameter optimization for the selected catalytic samples. Given that the selectivity of the Rh-based catalysts employed individually in the reductive amination of benzaldehyde exhibited a similar trend to that of the mechanical mixture with the Mo-based catalyst, the optimization of parameters for the reductive amination step was carried out by studying the Rh-based catalytic samples, excluding Mo(5%)-N/C.

The amount of the catalyst (Fig. 41) was the initial focus in the parameter optimization of this reaction due to the aforementioned rarity and cost associated with Rh.⁵¹

Rh(5%)-N/C. Tests were conducted by varying its quantity (while keeping the other parameters from Table 12 constant) from 25 to 75 mg to assess the influence on conversion and yield. Unsatisfactory outcomes were attained with a 25 mg of Rh(5%)-N/C (53% conversion) with low selectivity and no significant bias toward any of the desired products. Instead, 50 mg was selected as it resulted in complete conversion and the highest selectivity toward product (2) (53% selectivity, as previously mentioned). A higher amount of catalyst, on the other hand, resulted in reduced selectivity towards the desired secondary amine.

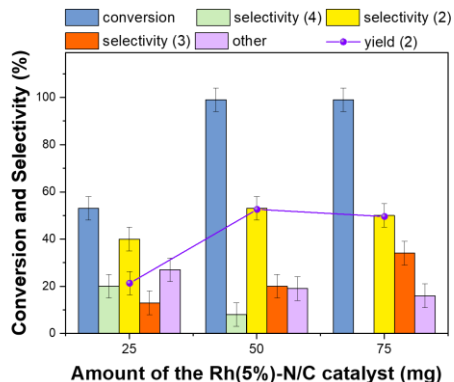


Figure 41: optimization of amount of Rh(5%)-N/C catalyst using reaction conditions of table 12.

Temperature was subsequently investigated within a range of 60 to 120 °C. The most favorable results, specifically for the secondary amine (2) with quantitative conversion and a 53% selectivity, were observed at 100 °C. At 60 °C, exceptionally high selectivity (86%) toward the imine (4) was observed, yet the conversion was low (38%), leading to an insufficient yield (33%) to be considered satisfactory. Further studies were required to determine the optimal conditions for achieving the

maximum yield for the imine (4).

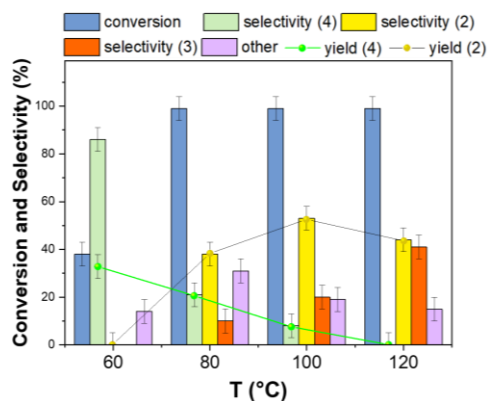


Figure 42: optimization of T (°C) using Rh(5%)-N/C.

H₂ Pressure was then investigated, employing the Rh(5%)-N/C sample and maintaining a temperature of 100 °C, within a range from 10 to 50 bar. The preferred product was (2), exhibiting a selectivity of approximately 53% at both 30 and 50 bar. Consequently, 30 bar was selected as the optimal hydrogen pressure in this case, for the formation of the secondary amine. Subsequently, Rh(3%)-N/C was tested using 50 bar of hydrogen in an attempt to increase the selectivity towards the tertiary amine (3), which is favored by an elevated concentration of ethylamine, the reduced product of ACN. This hypothesis proved to be correct, as the selectivity for (3) increased from 50% to 60%, as shown in Figure 43, establishing 50 bar as the optimal pressure for the synthesis of (3).

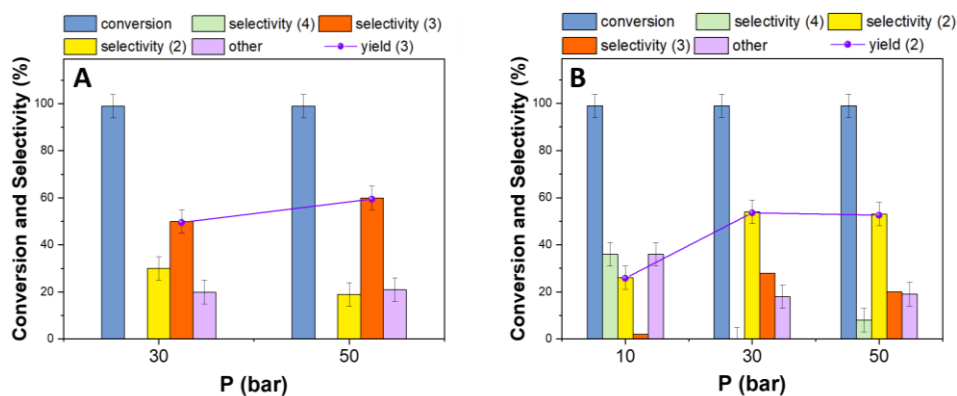


Figure 43: optimization of pressure for A): Rh(3%)-N/C and for B) Rh(5%)-N/C. the other conditions

are identical to those shown in Table 12.

Considering that during the temperature study, favorable selectivity toward the imine was achieved at lower temperatures (60 to 80 °C) and during the pressure investigation (yielding 36% selectivity at 10 bar), tests were conducted to identify the optimal reaction conditions for the imine (4). Therefore, at 80 °C, the pressure was varied from 10 to 50 bar using Rh(5%)-N/C, resulting in a selectivity of 54% toward (2) at 50 bar. The same selectivity for the amine (2) was achieved at 100 °C (instead of 80 °C) and 30 bar of H₂ (instead of 50 bar). It was decided to use 100 °C and 30 atm of hydrogen gas as the optimal values for the synthesis of (2), as the difference in pressure represents a greater safety hazard and economic cost compared to the difference in temperature. More importantly, at 80 °C and using 10 bar of H₂, a high selectivity of 72% was observed for the imine (4) with a conversion of benzaldehyde reaching 89%, resulting in a final yield of 64% for this compound, as shown in Figure 44.

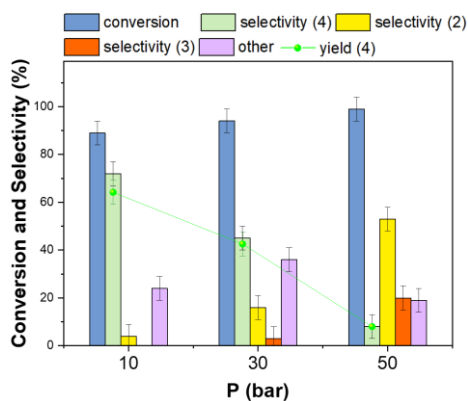


Figure 44: Pressure study at 80 °C to optimize imine (4) production using Rh(5%)-N/C.

The Volume of ACN, which was utilized both as a solvent and a reactant, was investigated using Rh(5%)-N/C within a range of 6 to 10 mL. The optimal results were obtained with 10 mL, resulting in a selectivity of 54% for (2), as depicted in Figure 45.

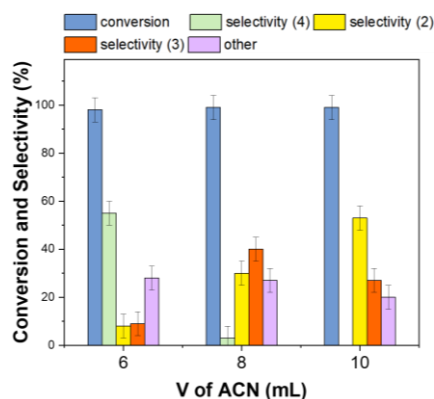


Figure 45: optimization of V of ACN using Rh(5%)-N/C.

Reaction time was examined using both the Rh(5%)-N/C and Rh(3%)-N/C samples, ranging from 4 to 24 hours, while maintaining the other reaction parameters specified in Table 14, except for the pressure (50 bar for Rh(3%)-N/C and 30 bar for Rh(5%)-N/C). Remarkably, quantitative conversion (>99%) was achieved even after 4 hours. While Rh(3%)-N/C had excellent selectivity at 4 h (55% for tertiary amine 3), for Rh(5%)-N/C, the selectivity towards the secondary amine after 4 and 12 hours resulted to be lower than 45%, rendering 24 hours as the optimal reaction time.

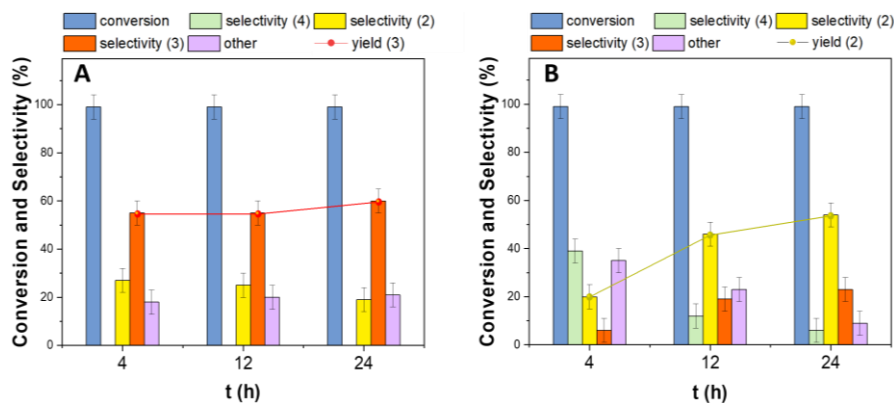
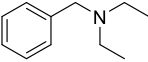
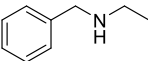
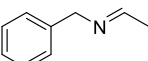


Figure 46: time optimization for A) Rh(3%)-N/C sample; B) Rh(5%)-N/C.

As a result of this investigation into the reaction parameters for the reductive amination of benzaldehyde, three different protocols have been identified and are documented in Table 13. Each of these protocols yields a reductive amination product, including the secondary and tertiary amines (2 and 3, respectively), as well as the imine (4).

Table 13: Summary of optimized reaction conditions for the reductive amination of benzaldehyde.

Volume of ACN were 10 mL for all the reported protocols.

Protocol	Catalyst	t (h)	T (°C)	P (bar)	Major product	Selectivity (%)*	Yield (%)*
1	Rh(3%)-N/C	4	100	50	 (3)	60	60
2	Rh(5%)-N/C	24	100	30	 (2)	54	54
3	Rh(5%)-N/C	24	80	10	 (4)	72	64

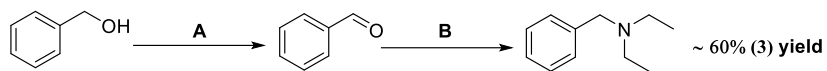
*: selectivity and yield were improved when using the mechanical mixture of Rh-based catalysts with Mo(5%)-N/C.

3.2.3. Tandem reactions.

Upon completing the optimization of both steps in the tandem reaction, the chosen strategy comprises: A) the selective oxidation of BnOH to benzaldehyde, utilizing the conditions outlined in Table 11, and B) the reductive amination of benzaldehyde in acetonitrile, resulting in three primary products: (3) following Protocol 1, (2) following Protocol 2, and (4) following Protocol 3 (Table 13). Throughout the investigations, mechanical mixtures of Rh(3%)-N/C and Rh(5%)-N/C with Mo(5%)-N/C, yielded the same optimal results as Mo(5%)-N/C alone in the initial oxidation step. Furthermore, they exhibited superior selectivity and yield for (3) and (2), respectively, in the reductive amination step (Fig. 40). The tandem reactions employed the strategies detailed in Table 14.

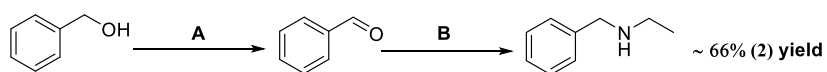
Table 14: Optimized strategies for the perfected tandem reactions.

STRATEGY 1): 50 mg of Rh(3%)-N/C mixed with 25 mg of Mo(5%)-N/C were used					
Oxidation (A)			Reductive Amination (B)		
T	P _{air}	t	T	P _{H₂}	t
170 °C	std. (1 atm)	18 h	100 °C	50 bar	4 h



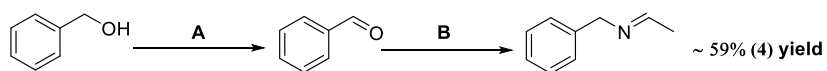
STRATEGY 2): 50 mg of Rh(5%)-N/C mixed with 25 mg of Mo(5%)-N/C were used

Oxidation (A)			Reductive Amination (B)		
T	P _{air}	t	T	P _{H₂}	t
170 °C	std. (1 atm)	18 h	100 °C	30 bar	24 h



STRATEGY 3): 50 mg of Rh(5%)-N/C mixed with 25 mg of Mo(5%)-N/C were used

Oxidation (A)			Reductive Amination (B)		
T	P _{air}	t	T	P _{H₂}	t
170 °C	std. (1 atm)	18 h	80 °C	10 bar	24 h



The results obtained are presented in Figure 47. In all three cases, the reaction solutions did not contain any traces of BnOH or benzaldehyde (1), indicating that both steps achieved a conversion rate exceeding 99%. Furthermore, the absence of benzoic alcohol (1b) in the solutions suggests that a quantitative selectivity of BnOH towards benzaldehyde was achieved in the first step.

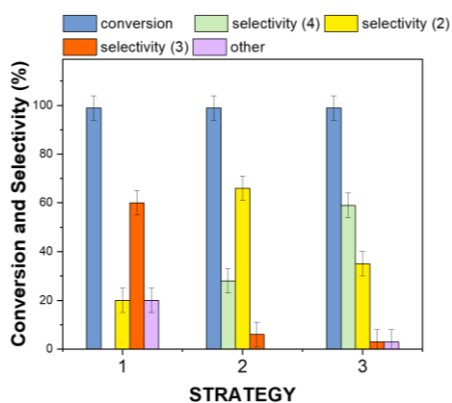


Figure 47: graphed data of the 3 strategies employed in tandem reactions comprising the oxidation of BnOH and the consecutive reductive amination of benzaldehyde (reaction conditions are as shown in Tab.16).

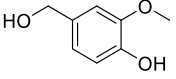
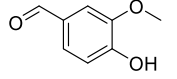
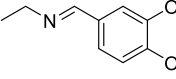
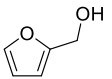
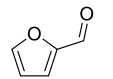
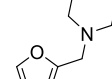
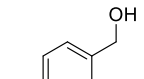
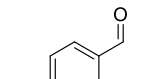
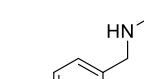
3.2.4. Substrate scope

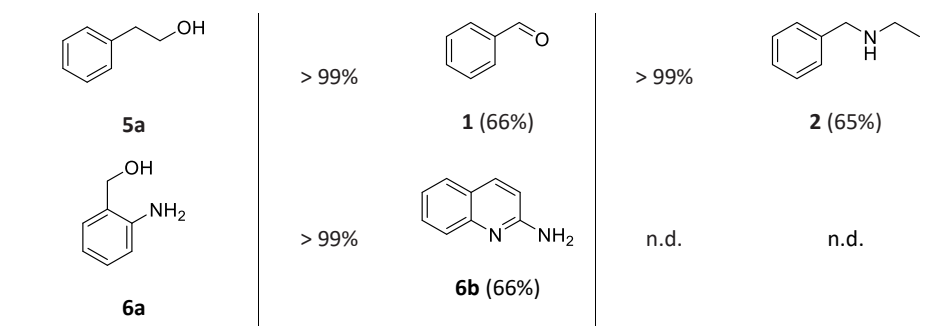
After developing these three strategies for the tandem reaction with BnOH as the model substrate, our efforts shifted towards assessing the catalytic system in tandem reactions involving the initial selective oxidation of biomass-derived aromatic alcohols (or derivatives) into their respective aldehydes, followed by the subsequent reductive amination reaction. To accomplish this, we considered the following substrates (displayed in Table 15) and employed the reaction conditions specified in Table 14. During the intermediate stage between the two steps, a small aliquot of the solution was extracted for further analysis.

Table 15: reaction conditions used for the substrate scope.

STRATEGY 2): 50 mg of Rh(5%)-N/C mixed with 25 mg of Mo(5%)-N/C were used					
Oxidation (A)			Reductive Amination (B)		
T	P _{air}	t	T	P _{H₂}	t
170 °C	std. (1 atm)	18 h	100 °C	30 bar	24 h

Table 18: Substrate scope.

Substrate	Oxidation (A)		Reductive Amination (B)	
	Conversion	Major product (& selectivity)	Conversion	Major product (& selectivity)
 2a	90%	 2b (>99%)	> 99%	 2c (93%)
 3a	> 99%	 3b (>99%)	95%	 3c (26%)
 4a	80%	 4b (>99%)	99%	 4c (53%)



2a: vanillyl alcohol, **2b:** vanillin, **2c:** 4-(Ethyliminomethyl)-2-methoxyphenol, **3a:** furfuryl alcohol, **3b:** furfural, **3c:** N-ethyl-N-(2-furylmethyl)ethanamine, **4a:** 4-Bromo benzylic alcohol, **4b:** 4-Br-benzaldehyde, **4c:** N-Ethyl-4-bromobenzylamine, **5a:** Phenylethyl alcohol, **1:** Benzaldehyde, **2:** Ethylbenzylamine, **6a:** 2-aminobenzyl alcohol, **6b:** imino quinoline.

Vanillyl alcohol (2a) showed good conversion and quantitative selectivity toward its aldehyde (vanillin, **2b**) which gave good selectivity towards the imine product **2c** (> 99% conversion and 93% selectivity), reaching an imine yield of 84%. This was a very promising result, hence, also considering that vanillyl alcohol and vanillin are solids at room temperature (their m.p. are both c.a. 82 °C), this substrate was chosen to design a mechanochemical protocol (which will be described in the next sections). Vanillin, the oxidized intermediate of this tandem reaction, is an extremely interesting compound, finding a broad range of applications, especially as flavoring molecule and as a building platform for pharmaceuticals synthesis (where reductive amination is a transformation of significant importance).⁵⁵ Vanillin can also find uses in polymeric synthesis.⁵⁶

Furfuryl alcohol (3a) showed good results in the oxidation step towards furfural (**3b**) (quantitative yield), however gave poor selectivity in the reductive amination step (only 26% selectivity for the tertiary amine). This result could certainly be improved through a thorough optimization of the reaction conditions, as demonstrated in the case of BnOH. In fact, the literature confirms that the selectivity toward this product can be enhanced to as high as 76%.⁵³

4-Bromo benzylic alcohol **4a** yielded quantitatively the aldehyde (**4b**), showing 53% selectivity toward the secondary amine (**4c**), which is a result entirely coherent with the results herein obtained for BnOH. The second most predominant product of the reductive amination of **4b** was the tertiary amine with 47% selectivity, indicating that a more thorough investigation of reaction conditions could potentially enhance selectivity.

Phenylethyl alcohol (5a), instead, displayed an unfavorable selectivity in the first step, leading to the production of benzaldehyde through oxidative cleavage. It is reasonable to assert that reducing the

temperature could enhance selectivity towards the desired aldehyde, as it was achieved with only 5% selectivity at 170 °C. The obtained benzaldehyde exhibited a similar trend to that observed in the reductive amination reaction.

2-aminobenzyl alcohol **6a** investigation was limited to the first stage of the tandem system, specifically the oxidation reaction. In this step, the formation of iminoquinoline (with 66% selectivity) was observed, resulting from the oxidative cyclization of the substrate with the reduced products of ACN, particularly ethylamine (as shown in Fig. 48). This selectivity was found to be influenced by the presence of Rh metal in the mechanically mixed catalyst, as experiments conducted without Rh resulted in the aldehyde becoming the major product (with 56% selectivity, compared to 15% when Rh was present). Furthermore, the selectivity for iminoquinoline decreased to 10% in the absence of Rh (as shown in Fig. 49). Another detected product was 2-(3-quinolinyl)aniline, formed through oxidative cyclization between two moles of the substrate **6a**.⁵⁷

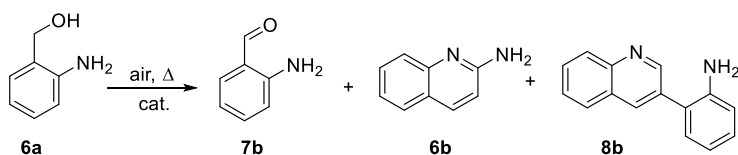


Figure 48: scheme of the reaction pathway of the oxidation of **6a**. **6a**: 2-aminobenzyl alcohol; **7b**: 2-aminobenzaldehyde; **6b**: iminoquinoline; **8b**: 2-(3-quinolinyl) aniline.

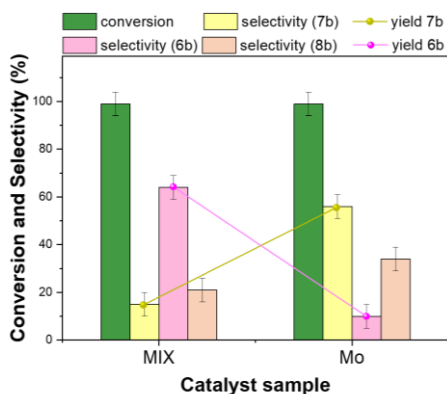


Figure 49: oxidation reaction of **6a** using mechanically mixed Rh(5%)-N/C with Mo(5%)-N/C (MIX), compared with using Mo(5%)-N/C alone (Mo).

When performing the oxidation reaction of **6a** using only Mo(5%)-N/C, the desired aldehyde **7b** was obtained with c.a. 56% yield. Subsequently, Rh(5%)-N/C was introduced in the system to study the

reductive amination, yielding the imine product **6c** with selectivity higher than 99%, albeit with 36% conversion (Fig. 50).

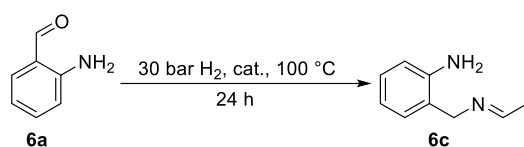


Figure 50: reaction pathway for the reductive amination of **6a**.

3.2.1. Catalyst reusability

The costs associated with the catalyst in a liquid-phase reaction can account for as much as one-third of the overall process cost. Therefore, any loss of the catalyst due to leaching or other factors is highly significant, underscoring the importance of its recovery and reuse.¹⁷ To assess the stability and reusability of both Mo(5%)-N/C and Rh(5%)-N/C catalytic samples, recycling experiments were designed under the reaction conditions outlined in Protocol 2 (Table 14). After the completion of a reaction cycle, the catalysts, in each case, were separated through filtration, rinsed with 30 mL of acetone, and left to dry overnight.

The recovered catalysts were added into fresh solutions containing the corresponding substrate (1 mmol) and acetonitrile (10 mL), and new reactions (oxidation and reductive amination, respectively) were initiated. The recycling process was repeated six times for Mo(5%)-N/C in the oxidation of BnOH and six times for Rh(5%)-N/C in the reductive amination of benzaldehyde. The entire series of reactions was performed twice to ensure reproducibility. The results are depicted in Figure 51.

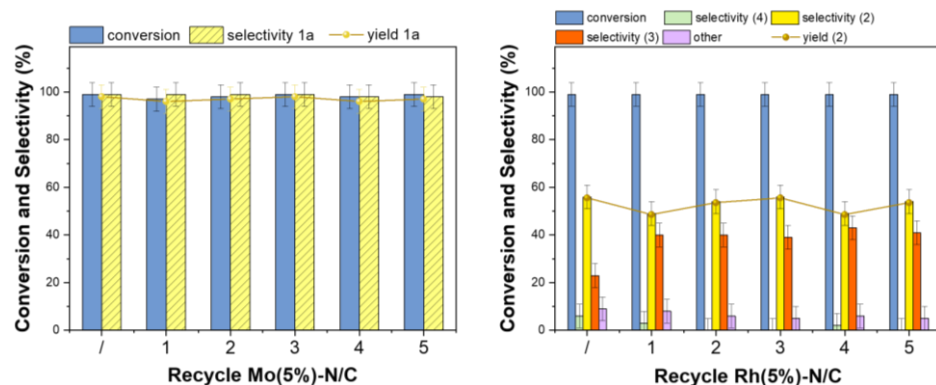


Figure 51: Catalyst reusability study. On the left: Mo(5%)-N/C recycles in the oxidation of BnOH; On the right: Rh(5%)-N/C recycles in the reductive amination of benzaldehyde.

As seen in Figure 51, both catalytic samples maintained consistent conversion and selectivity over the course of six uses in their respective reactions. This indicates that the overall performance of Mo(5%)-N/C and Rh(5%)-N/C was not affected by the reaction environment or the recycling process, with only minor variations observed in the selectivity towards the secondary amine in the case of the reductive amination reaction.

3.2.2. Post-recycle characterization.

A post-characterization analysis of Mo(5%)-N/C and Rh(5%)-N/C was conducted to gain insights into the chemical, structural, and morphological features of the samples after the catalytic reactions and their reuse, under the previously reported conditions. For this purpose, the same multi-technique approach previously described for the fresh catalytic samples was used. Thus, analyses were performed using XRD, N₂-physisorption, XPS, and TEM techniques.

The analysis of the data obtained from these investigations will be provided in the subsequent sections. Firstly, we will delve into the discussion of the Mo(5%)-N/C sample, as depicted in Figure 52 and Figure 53:

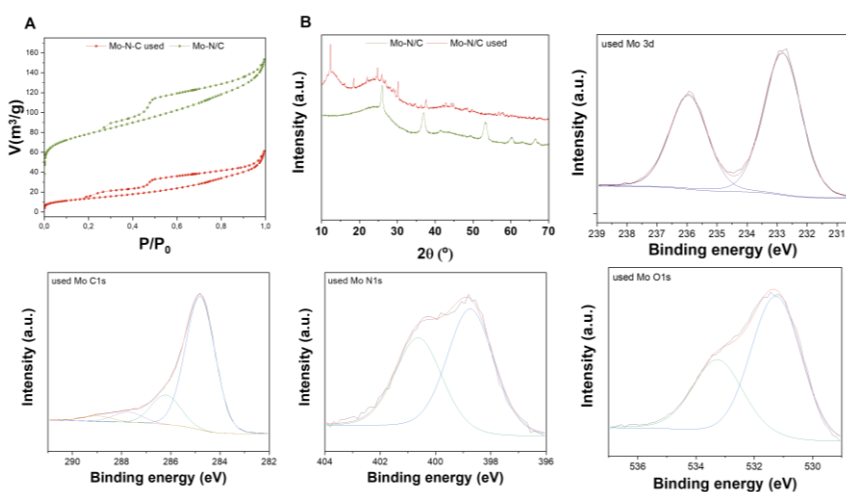


Figure 52: complete characterization of the used Mo(5%)-N/C sample. **A)** compared isotherms of used Mo-N/C and fresh Mo-N/C samples; **B)** compared XRD spectra of used Mo-N/C and fresh Mo-N/C samples. The remaining graphs are the XPS results of Mo 3d, C 1s, N 1s, O 1s of the used Mo-N/C sample accordingly to the depicted order.

Commentato [DRP1]: The xrd graph should be improved, spacing both patterns

Commentato [DRP2]: It is needed to label them all, from A to F

As depicted in Figure 52A, the N₂-physorption isotherms indicated that the used material maintained a mesoporous structure, as evidenced by typical Type IV isotherms with Type II adsorption hysteresis. However, a significant reduction in the adsorbed volume, as compared to the fresh sample, was observed (as indicated in Table 16), resulting in a surface area of 50 m²/g, which is only 17% of the initial value of the fresh sample. The pore volume, measuring 0.07 cm³/g, was three times lower than that of the fresh sample, while the average pore diameter (5.6 nm) nearly doubled. These results were consistent with our expectations, as the adsorption of organic substances can result in the obstruction of smaller pores.

Table 16: N₂-physorption analysis of fresh Mo(5%)-N/C and used Mo(5%)-N/C samples.

Material Sample	S _{BET} [m ² /g] ^a	D _{BJH} [nm] ^b	V _{BJH} [cm ³ /g] ^c
Fresh Mo(5%)-N/C	285	2.9	0.21
Used Mo(5%)-N/C	49	5.6	0.07

a: S_{BET}: specific surface area was calculated by the Brunauer-Emmett-Teller (BET) equation.

b: D_{BJH}: mean pore size diameter was calculated by the Barret-Joyner-Halenda (BJH) equation.

c: V_{BJH}: pore volumes were calculated by the Barret-Joyner-Halenda (BJH) equation.

The XRD patterns of the used Mo-N/C sample showed significant differences from the results of the fresh Mo-N/C sample (Figure 52 B). The spent catalytic material exhibited new signals and a larger degree of amorphization. A sharp signal at 13° was observed in the XRD pattern, together with the decay of the signal at 51°. These changes indicate the nearly complete oxidation of Mo species, transitioning from a mixture of MoO₂ and MoO₃ mixture to a prevalent MoO₃ matrix.

HRTEM-EDX analyses and HRTEM micrographs (Figure 53) of the re-used Mo-N/C sample, did not exhibit considerable differences when compared to the fresh sample. The mean particle diameter was calculated to be around (30±2) nm, which was very similar to the value of (31±2) nm observed for the fresh material. HRTEM-EDX analysis also revealed a remarkably uniform distribution of the active molybdenum sites. These sites maintained excellent dispersion without any signs of agglomeration, indicating that sintering did not occur during the repeated reactions.

Commentato [DRP3]: To revise the real calculated value

Commentato [DRP4]: In the figure modify micrographics for micrographs

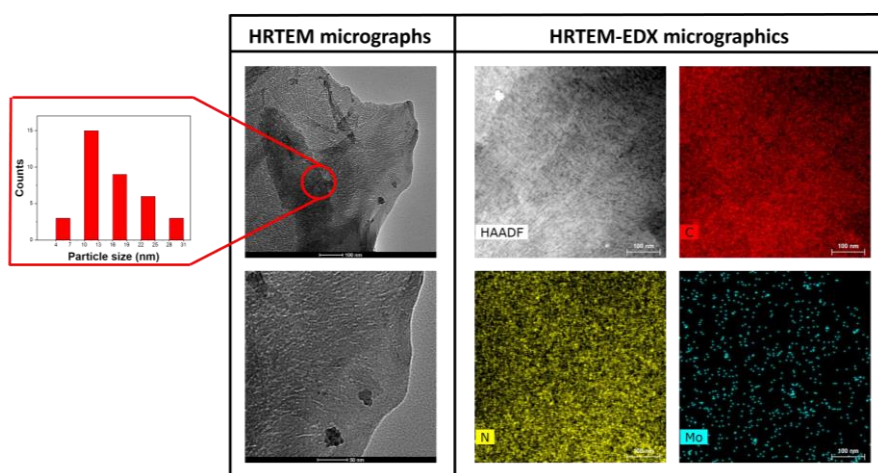


Figure 53: *on the left:* HRTEM micrographs of the Mo(5%)-N/C used sample; *on the right:* HRTEM-EDX micrographics of the Mo(5%)-N/C used sample.

XPS analysis of the used Mo-N/C material is reported in Figure 52. The most significant difference observed in the XPS spectra, in comparison with the fresh Mo-N/C sample (depicted in Figure 18, C) is observed in the Mo 3d region. The signals at 232.7 and 235.9 eV were attributed to Mo(VI) species, hinting that MoO₃ was the major phase in the used sample. This corroborates the XRD data, which also demonstrated the complete oxidation of the active metal during the studied reaction. The C 1s, N 1s, and O 1s spectra (Figure 52) did not display significant differences with respect to the same contributions in the XPS data of the fresh material (Figure 18). This study has revealed that during its use, the Mo(5%)-N/C sample underwent textural, morphological, and chemical alterations, none of which adversely impacted its catalytic performance. The consistent size of the metal nanoparticles appears to be a critical factor in maintaining the system efficiency over time. Moving forward, the subsequent paragraphs will center on the post-recycle characterization of the Rh(5%)-N/C sample after multiple recycling cycles (Figure 54, Figure 55).

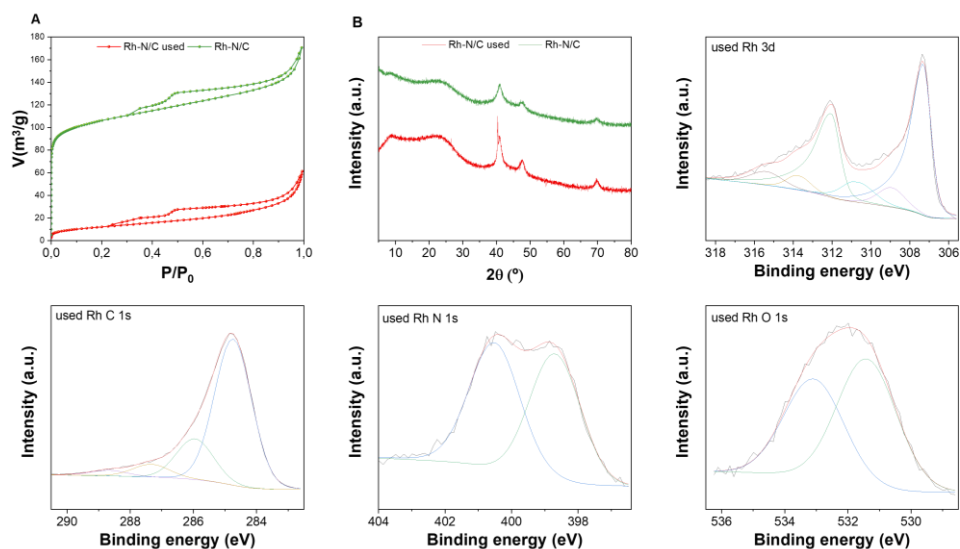


Figure 54: complete characterization of the used Rh(5%)-N/C sample. **A)** compared isotherms of used Rh-N/C and fresh Rh-N/C samples; **B)** compared XRD spectra of used Rh-N/C and fresh Rh-N/C samples. The remaining graphs are the XPS results of Mo 3d, C 1s, N 1s, O 1s of the used Rh-N/C sample accordingly to the depicted order.

Commentato [DRP5]: Add also C-F labels

As shown in Figure 54 A), the N_2 -physorption analysis revealed that the used material retained a mesoporous behaviour, since it exhibited typical Type IV isotherms with Type II adsorption hysteresis. However, a drastic reduction in the adsorbed volume, even more pronounced than that observed in the case of the Mo(5%)-N/C sample, was evident when compared to the fresh sample (as indicated in Table 19). Consequently, there was also observed a reduction in the surface area down to $44 \text{ m}^2/\text{g}$, which represents only 9% of the initial value of the fresh sample. The pore volume of $0.06 \text{ cm}^3/\text{g}$ was almost 4 time lower than that of the fresh sample, while the mean pore diameter (5.5 nm) showed a lower value than the fresh sample (6.5 nm), contrarily to what happened with the Mo-N/C sample. These results can be explained by a collapse of the internal structure of the carbonaceous materials, resulting in both smaller pores and less surface area.

Table 19: N_2 -physorption parameters of fresh Rh(5%)-N/C and used Rh(5%)-N/C samples.

Material Sample	$S_{\text{BET}} [\text{m}^2/\text{g}]^{\text{a}}$	$D_{\text{BJH}} [\text{nm}]^{\text{b}}$	$V_{\text{BJH}} [\text{cm}^3/\text{g}]^{\text{c}}$
Fresh Rh(5%)-N/C	489	6.5	0.23

Used Rh(5%)-N/C

44

5.5

0.06

a: S_{BET} : specific surface area was calculated by the Brunauer-Emmett-Teller (BET) equation.

b: D_{BJH} : mean pore size diameter was calculated by the Barret-Joyner-Halenda (BJH) equation.

c: V_{BJH} : pore volumes were calculated by the Barret-Joyner-Halenda (BJH) equation.

The XRD patterns of the used Rh(5%)-N/C sample exhibited minor differences when compared to the XRD spectrum of the fresh Rh(5%)-N/C sample. Particularly, three peaks were identified in the used sample, at 41°, 48°, and 70°, in accordance with the typical diffractions associated with the (111), (200), and (220) crystalline planes of metallic Rh, also found in the fresh sample. This confirms the presence of metallic Rh in the used catalyst. In addition to these observations, it can be noted that the sample maintained an amorphous structure, as indicated by the broad nature of the peaks. HRTEM-EDX analyses and HRTEM micrographs (Figure 55) of the re-used Rh(5%)-N/C sample did not exhibit significant changes as compared to the fresh sample, given that the mean particle diameter was calculated to be around (6.0 ± 2.0) nm, while it was (5.9 ± 2.0) nm for the fresh material. HRTEM-EDX results also demonstrated a homogeneous distribution of the active rhodium sites, maintaining a good dispersion. However, there were some agglomerated regions that likely contributed to the increase in the mean particle diameter.

Commentato [DRP6]: Always use the same significant numbers for the same kind of data, in this case, or 41 or 41.0, but consistent all over the manuscript

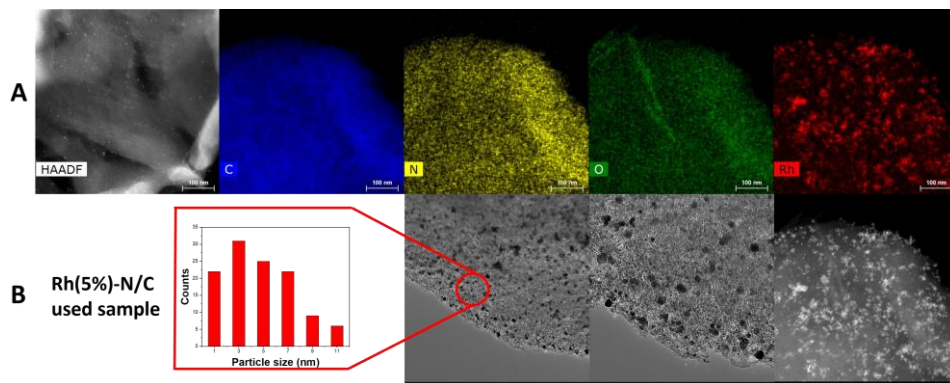


Figure 55: A) HRTEM-EDX micrographics of the Rh(5%)-N/C used sample. B): HRTEM micrographs of the Rh(5%)-N/C used sample.

XPS analysis of the Rh-N/C used material is reported in Figure 54. No significant differences were observed when comparing the XPS regions of the fresh Rh(5%)-N/C and used Rh(5%)-N/C. In the Rh 3d XPS region of the used sample, peaks characteristic of both Rh⁰ and Rh³⁺ were detected with no

shift of binding energy from the fresh sample. Furthermore, the presence of additional contributions at around 310.7 and 315.4 eV, akin to the fresh sample, strongly indicates that the Rh-N bonds did not were affected, most likely contributing to the stability of the samples, thereby preventing leaching during the catalytic transformations. This study highlighted that during its utilization, the Rh(5%)-N/C sample underwent textural, and structural modifications, but none of these changes affected its catalytic performance. This study revealed that while the Rh(5%)-N/C sample underwent alterations, in terms of textural, and structural features, during use, none of these changes had an adverse impact on its catalytic performance.

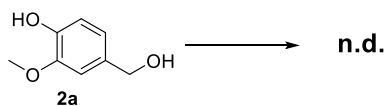
3.2.3. Mechanochemical perspectives

As previously discussed in the introduction, while solvents play a crucial role in the chemical industry, they also present significant challenges related to health and safety, environmental impact, regulatory compliance, and cost management. Proper risk assessment, safety measures, and sustainable practices are essential to address these challenges effectively. Even more, the design of solvent free protocols for organic transformations is a thrilling and challenging goal, which has recently spurred the scientific community to explore solventless mechanochemical protocols for the preparation of chemicals and materials.

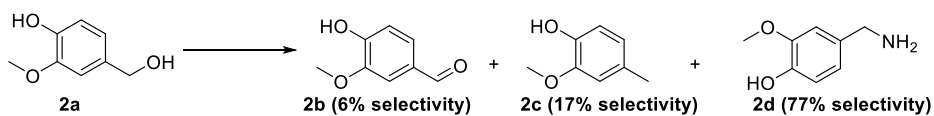
Inspired by such premises, the final stage of this Thesis was dedicated to evaluate the catalytic performance of the synthesized materials (Mo-N/C) through mechanochemically-assisted oxidation reactions. More specifically, a continuous-flow solvent-free protocol was developed using a mini-twin screw extruder to produce vanillin through the selective oxidation of vanillyl alcohol. This particular reaction was selected for implementation within the mechanochemical strategy from the range of reactions examined during the substrate scope investigation. The choice was influenced by the fact that both the starting material, vanillyl alcohol, and the desired product, vanillin, possess melting points significantly above room temperature (115°C and 83°C, respectively).⁵⁸ This characteristic makes them suitable candidates for a solvent-free mechanochemical approach.

During this investigation, we delved into the capabilities of three different oxidizing agents, namely air, hydrogen peroxide and urea hydroperoxide. Air, given its affordability, safety, and widespread availability, seemed to be the most promising choice. However, contrary to our expectations, it failed to deliver the desired outcomes as it did not lead to any conversion of vanillyl alcohol. (Fig. 57, A).

A) Air as the oxidant: **conversion = 0%**



B) Urea hydrogen peroxyde as the oxidant: **conversion = 70%**



C) H₂O₂ as the oxidant: **conversion = 95%**

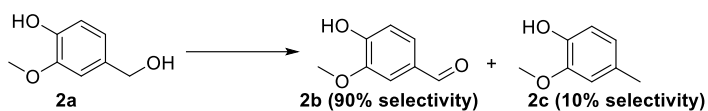


Figure 57: schematic representation of the oxidation of vanillic alcohol using **A)** air, **B)** urea peroxide, **C)** hydrogen peroxide. **2b:** vanillin, **2c:** creosol, **2d** vanillyl amine.

Secondly, following a literature review to identify a suitable solid oxidizing agent, urea hydroperoxide (as indicated in Table 20) was chosen. This selection was based on its relatively low melting point (up to 95 °C)⁵⁸ and its environmentally friendly characteristics when compared to other solid oxidants. Many solid inorganic oxidants, such as potassium permanganate, are known for their high toxicity and environmental pollution, making urea hydroperoxide a more sustainable choice.⁵⁹ Urea hydroperoxide, exhibited a favorable conversion rate of 70%. However, it fell short in terms of selectivity towards vanillin, achieving only 6%. Surprisingly, the primary amine **2d** emerged as the major product in this scenario (as depicted in Figure 57,**B**). In any case, these findings were exceptionally intriguing and have the potential to unlock new avenues for the synthesis of amine-containing compounds using solventless mechanochemical approaches.

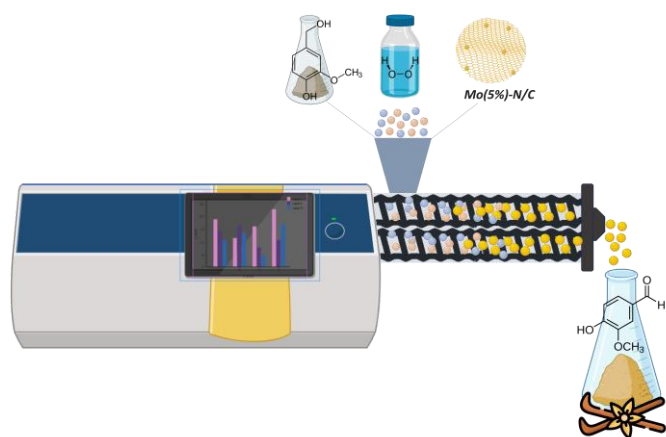
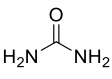


Figure 58. Schematic representation of the mechanochemical synthesis of vanillin.

On the other hand, hydrogen peroxide delivered the most promising outcomes, boasting an impressive 95% conversion rate and remarkable selectivity towards vanillin, reaching 90% (equivalent to an approximate 86% yield) (Figure 58). It is important to note that hydrogen peroxide, although introduced in liquid form, gave rise to a slurry-like reaction mixture when combined with the reagent and catalyst under the specified conditions. This transformation mimicked a SLAG working condition, characteristic of a mechanochemical protocol (as illustrated in Fig. 57 C). Consequently, hydrogen peroxide emerged as the optimal oxidizing agent for this particular reaction. For a visual representation of all three reaction pathways, refer to Fig. 57, and for detailed reaction conditions, consult Table 20. While these are preliminary findings, the promising results obtained in this study will undoubtedly lay the groundwork for more extensive investigations within our research group in this particular field in the near future.

Table 20: reaction conditions for the mechanochemical tests, *2a: Vanillic alcohol.

Catalyst sample (amount)	2a amount	Oxidizing agent (amount)	T °C	rpm	t h
Mechanical mix (75 mg) Rh(5%)-N/C (50 mg) + Mo(5%)-N/C (25 mg)	2 g (18 mmol)	H ₂ O ₂ hydrogen peroxide (1.2 eq)	80	100	1
Mechanical mix (75 mg) Rh(5%)-N/C (50 mg) + Mo(5%)-N/C (25 mg)	2 g (18 mmol)	 H ₂ O ₂ urea peroxide (2.5 eq)	80	100	1
Mechanical mix (75 mg) Rh(5%)-N/C (50 mg) + Mo(5%)-N/C (25 mg)	2 g (18 mmol)	air	80	100	1

4. Application of the Green Metrics of the CHEM21 toolkit

In the final section of this Thesis, the developed protocols will be evaluated using the previously introduced CHEM21 toolkit Zero Pass, to quantify the greenness of the newly introduced process. The processes which will be examined are the 3 strategies developed in the tandem reactions divided in 2 steps each, namely the selective oxidation of benzyl alcohol to benzaldehyde and the consecutive reductive amination of the latter. Moreover, the mechanochemical strategy to yield vanillin from vanillic alcohol will be evaluated using green chemistry metrics.

CHEM21 toolkit will be applied to the mentioned processes using an effective approach, aimed at establishing a reference system capable of putting all the green metrics encompassed in the Zero Pass in the toolkit. This approach has its operating principle of remodeling the green metrics so that they give values from 0 to 1, 0 being the worst outcome in terms of greenness, and 1 being the best. This strategy is inspired to that brought forward with the inclusion of environmental impact parameters in the radial pentagon of Andraos.⁶⁰

In the following Table 21, the remodeled green chemistry metrics of Zero Pass will be shown, with the exception of Mass Intensity (MI), which is a parameter that opposes in nature to the other displayed metrics. The value of MI can not be converted in a percentage, since it represents the total mass introduced in the process (in kgs) to yield 1 kg of product, thus it does not fall in a delimited range. For this reason, MI will be displayed as it is shown in Table 6, separately from the

other values of Table 21, which will be converted in a hexagon radial diagram, in which values near 1 will be considered excellent, while values near 0 will indicate poor greenness of the process.

Table 21: formulas for the remodeled described green metrics parameters of the First Pass of the toolkit⁵¹ that will be included in the hexagon of each examined process.

$$\text{Percentage yield} = \frac{\text{moles of product}}{\text{moles of limiting reactant}}$$

$$\text{Percentage conversion (C)} = 1 - \left(\frac{\text{final mass of limiting reactant}}{\text{initial mass of limiting reactant}} \right)$$

$$\text{Percentage selectivity (S)} = \frac{\% \text{yield}}{\% \text{conversion}}$$

$$\text{AE} = \frac{\text{molecular weight of products}}{\text{total molecular weight of reactants}}$$

$$\text{RME} = \frac{\text{mass of isolated product}}{\text{total mass of reactants}}$$

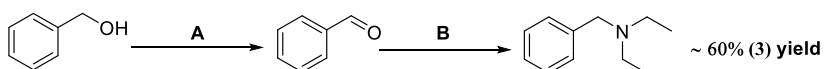
$$\text{OE (optimum efficiency)} = \frac{\text{RME}}{\text{AE}}$$

Tandem reactions shown in table 14 will be discussed dividing them in each step: **A** for oxidation of BnOH and **B** for the reductive amination of benzaldehyde. Table 14 will be shown for simplicity.

Table 14: Optimized strategies for the perfected tandem reactions.

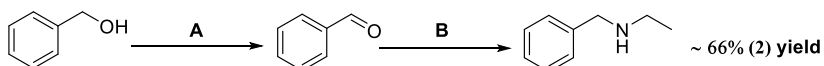
STRATEGY 1): 50 mg of Rh(3%)-N/C mixed with 25 mg of Mo(5%)-N/C were used

Oxidation (A)			Reductive Amination (B)		
T	P _{air}	t	T	P _{H₂}	t
170 °C	std. (1 atm)	18 h	100 °C	50 bar	4 h



STRATEGY 2): 50 mg of Rh(5%)-N/C mixed with 25 mg of Mo(5%)-N/C were used

Oxidation (A)			Reductive Amination (B)		
T	P _{air}	t	T	P _{H₂}	t
170 °C	std. (1 atm)	18 h	100 °C	30 bar	24 h



STRATEGY 3): 50 mg of Rh(5%)-N/C mixed with 25 mg of Mo(5%)-N/C were used

Oxidation (A)			Reductive Amination (B)		
T	P _{air}	t	T	P _{H₂}	t
170 °C	std. (1 atm)	18 h	80 °C	10 bar	24 h

~ 59% (4) yield

It should be noted that step A of all three strategies is identical, thus its evaluation according to green chemistry metrics will be done once to avoid redundancy.

Step A) of **STRATEGY 1, STRATEGY 2, STRATEGY 3:**

On the left, the hexagon chart applied to the optimized oxidation of BnOH with the green metrics of Table 21 is displayed. As it can be seen, step A of the devised strategies (1, 2, and 3) presents excellent results for the metrics included in the Zero Pass of the CHEM21 toolkit. All values are proximate to 1, the maximum.

Moreover, MI resulted to be: $MI = 1,02$

This means that this process needs 1,02 kg of inserted mass in the system, to yield 1 kg of product, which is an excellent value.

It is needed to mention that ACN is solely a solvent in step A of the three developed

strategies, and normally it should be considered in calculating MI. However, it is both solvent and reactant for the consequent reaction step. This makes considering the utilized mass of ACN troublesome since, it can easily be recycled and replenished as it is consumed in the step B of the tandem reactions. If considered it would give a value of MI of 74,79 kg of needed mass to yield 1 kg of product, which does not truly represent this process.

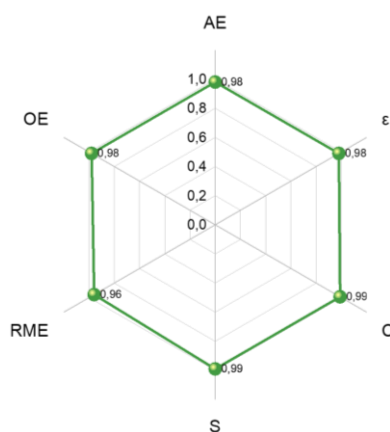


Figure 59: hexagon radial chart comprising CHEM21 Zero Pass metrics applied to Part A of **STRATEGY 1, 2, and 3.**

Step B) of **STRATEGY 1**:

On the left, the hexagon chart with the Green Chemistry metrics of Table 21 is displayed.

Differently than the results for step A, step B shows lower values of the examined parameters, meaning that this step lacks under certain aspects.

Selectivity proved to be the major hindering factor, since being only 60%, it lowers yield towards the desired product (tertiary amine 3) and intrinsically increases waste. This is confirmed by the difference between AE (ca. 70%) and RME. RME is a metric which is similar to AE, although it also takes in consideration selectivity and stoichiometric excess of reagents, resulting in being almost half of AE.

While yield was the biggest factor in affecting RME, the stoichiometric factor (SF) also played a major role, due to the excess of hydrogen gas introduced in the system. This excess was necessary to push selectivity towards the tertiary amine (3) and, while on a laboratory scale the residual hydrogen gas was purged, it could be recovered and reused(?). This could raise RME to better values. In this step, as in step A and all other strategies' step B), ACN as a reagent was not considered in excess, while it was considered as a solvent, albeit with the possibility to recycle it, resulting in a MI = 4.5. MI's value is higher than in step A because in this case ACN was considered both as reagent and solvent.

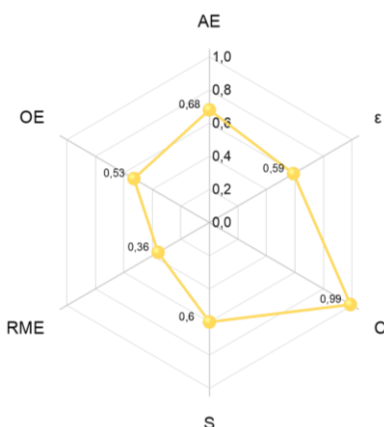


Figure 60: hexagon radial chart comprising CHEM21 Zero Pass metrics applied to **STRATEGY 1 Part B**.

Step B) of STRATEGY 2:

On the left, the hexagon chart with the Green Chemistry metrics of Table 21 is displayed.

The results of the metrics applied to part B of strategy 2 confirm that the major limiting factor of the reductive amination steps is the low yield. Moreover, since 1 less mole of ACN was needed to synthesize 1 mole of product compared to Part B of STRATEGY 1, AE is considerably higher in this case (ca. 90%). More specifically, in STRATEGY 1, to produce the tertiary amine 3, either the secondary amine diethyl amine (7, in Fig. 14) was needed to react with the substrate (Benzaldehyde), or an additional mole of ethyl amine reacted with the secondary amine (2), implying that the loss of one mole of ammonia (NH_3) was needed per mole of 7 produced in both mechanisms.

In strategy 2, the target product is the secondary amine 2, which is produced by the reaction between ethyl amine (which needs only two moles of H_2 to react with ACN) and the substrate, thus not including the loss of an ammonia molecule. The difference in production of secondary and tertiary amines from ACN was already discussed during the catalytic activity evaluation chapter.

MI was also improved because of ACN, since, while in both cases the V of solvent used is the same (10 mL), in this strategy the desired product (secondary amine 2) is produced consuming 1 less mole of ACN per mole of limiting reactant (Benzaldehyde), thus it consumes less mass per kg of final product. $\text{MI} = 3.6$.

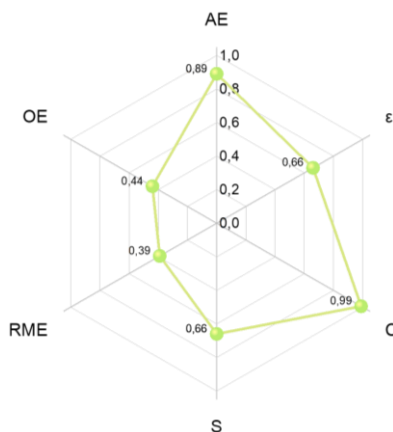


Figure 61: hexagon radial chart comprising CHEM21 Zero Pass metrics applied to Part B of STRATEGY 2.

Step B) of **STRATEGY 3**:

On the left, the hexagon chart with the Green Chemistry metrics of Table 21 is displayed. These results are similar to those of STRATEGY 2, Part B, since the mole of ACN needed to yield one mole of desired product is 1. Thus, the reason on the difference in AE compared to STRATEGY 1, Part B, has the same roots. Compared to STRATEGY 2, Part B, selectivity is lower, affecting yield, RME, and OE, making their values lower too. Considerations on ACN as the solvent are identical to what previously stated. $MI = 1.9$.

MI is lower than that of STRATEGY 1 and 2, mainly because of the difference in hydrogen pressure employed, which is 1/3 and 1/5 of that of the other 2 strategies.

Yield and selectivity are both Green flags for all steps A of the three strategies (>89%), while in steps B are all red (<70%) with only Part B of STRATEGY 2 being near to be an amber flag (70-89%) with 66% selectivity and yield.

Considering the discussion about the solvent used, ACN falls in the “problematic” solvent category according to the criteria proposed by CHEM21 toolkit (Table 5), but it should be noted that it serves a double purpose, as it is also a reactant in the second step of the tandem reactions. It is also easy to recycle and reuse for multiple reactions, so its impact can be lowered. Its toxicity is the biggest downside of using it in a synthetic route, as it was previously described in this Thesis.

While step A) of each strategy showed excellent results, the use of ACN was still a negative aspect of this process since it received a low rating because of its toxicity. This changed when considering the solvent-free mechanochemical for a continuous-flow production of vanillin from vanillyl alcohol through extrusion.

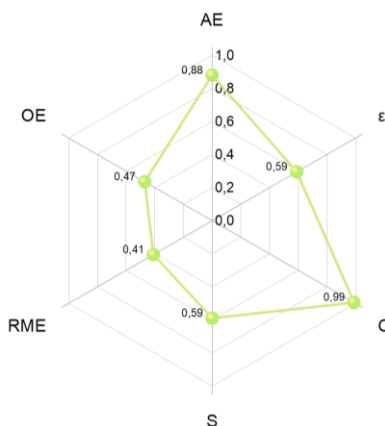


Figure 62: hexagon radial chart comprising CHEM21 Zero Pass metrics applied to Part B of **STRATEGY 3**.

As it is illustrated in Fig. 63, the green metrics of CHEM21 Zero Pass' toolkit were applied to the mechanochemical extrusive oxidation reaction of vanillyl alcohol to vanillin and the hexagon graph shows excellent results. Unfortunately yield and selectivity are not quantitative, but still both high enough to score a green flag for selectivity, and an amber for yield according to the toolkit. The other reason why the values of the metrics are not all near to 1 is that H₂O₂ was used in a slight excess (1.2 eq) to the limiting reactant (vanillyl alcohol).

It should be noted that even considering this excess, hydrogen peroxide is a green oxidant that yield water as a co-product of oxidation, thus it does not produce toxic waste in the reaction media. Lastly but most importantly, while it is true that ACN can be recycle in the previously discussed process, the recovering process consumes energy, and while its dispersion in the environment can be controlled, a potential leak can cause severe pollution and represents a safety hazard. In this mechanochemical process no ACN was used, bringing the MI at 1.28 kg of mass needed to yield 1 kg of product, contrary of the potential 74.79 kg in the oxidation process of BnOH to Benzaldehyde in ACN.

This was the only process to reach all green flags according to the CHEM21 Zero Pass toolkit.

A summary will be shown in the following Table 22.

Table 22: summary of the CHEM21 Zero Pass toolkit flag system applied to the devised processes.

Process	Yield	Selectivity	Solvent
Part A (STRATEGIES 1, 2, 3)	99%	99%	Problematic
Part B STRATEGY 1	60%	60%	Problematic
Part B STRATEGY 2	66%	66%	Problematic
Part B STRATEGY 3	59%	59%	Problematic
Mechanochemical approach	86%	90%	Absent

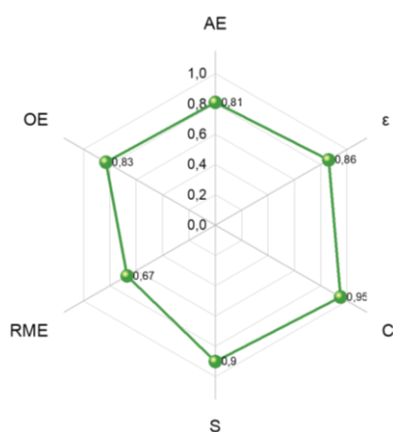


Figure 63: hexagon radial chart comprising CHEM21 Zero Pass metrics applied to the mechanochemical oxidation of vanillyl alcohol.

References:

- 1 U.S. Energy Information Administration - EIA - Independent Statistics and Analysis, <https://www.eia.gov/outlooks/archive/aeo21/>, (accessed September 12, 2023).
- 2 Y. M. Bar-On, R. Phillips and R. Milo, *Proceedings of the National Academy of Sciences*, 2018, **115**, 6506–6511.
- 3 L. D. Mthembu, D. Lokhat, R. Gupta and N. Deenadayalu, *Waste Biomass Valor*, 2021, **12**, 3179–3191.
- 4 Chemical Routes for the Transformation of Biomass into Chemicals | Chemical Reviews, <https://pubs.acs.org/doi/10.1021/cr050989d>, (accessed September 12, 2023).
- 5 FAOSTAT, <https://www.fao.org/faostat/en/#data/RL/visualize>, (accessed September 12, 2023).
- 6 Recent advances in the valorization of plant biomass | Biotechnology for Biofuels and Bioproducts | Full Text, <https://biotechnologyforbiofuels.biomedcentral.com/articles/10.1186/s13068-021-01949-3>, (accessed September 14, 2023).
- 7 H. Kargbo, J. S. Harris and A. N. Phan, *Renewable and Sustainable Energy Reviews*, 2021, **135**, 110168.
- 8 R. Bosch, M. van de Pol and J. Philp, *Nature*, 2015, **523**, 526–527.
- 9 M. Tayyab, *Appl. Ecol. Env. Res.*, 2018, **16**, 225–249.
- 10 C. Peral, in *Biotransformation of Agricultural Waste and By-Products*, eds. P. Poltronieri and O. F. D'Urso, Elsevier, 2016, pp. 125–160.
- 11 M. Pedersen and A. S. Meyer, *New Biotechnology*, 2010, **27**, 739–750.
- 12 K. Triantafyllidis, A. Lappas and M. Stöcker, *The Role of Catalysis for the Sustainable Production of Bio-fuels and Bio-chemicals*, Newnes, 2013.
- 13 S. Pugh, R. McKenna, I. Halloum and D. R. Nielsen, *Metabolic Engineering Communications*, 2015, **2**, 39–45.
- 14 T. Werpy and G. Petersen, *Top Value Added Chemicals from Biomass: Volume I -- Results of Screening for Potential Candidates from Sugars and Synthesis Gas*, 2004.
- 15 L. Filiciotto and R. Luque, *Current Green Chemistry*, 2018, **5**, 47–59.
- 16 T. Maschmeyer, R. Luque and M. Selva, *Chemical Society Reviews*, 2020, **49**, 4527–4563.
- 17 D. Polidoro, D. Ballesteros-Plata, A. Perosa, E. Rodríguez-Castellón, D. Rodríguez-Padrón and M. Selva, *Catal. Sci. Technol.*, 2023, **13**, 2223–2238.

- 18 F. Shahidi, J. K. V. Arachchi and Y.-J. Jeon, *Trends in Food Science & Technology*, 1999, **10**, 37–51.
- 19 K. V. Harish Prashanth and R. N. Tharanathan, *Trends in Food Science & Technology*, 2007, **18**, 117–131.
- 20 D. Polidoro, D. Ballesteros-Plata, A. Perosa, E. Rodríguez-Castellón, D. Rodríguez-Padrón and M. Selva, *Catal. Sci. Technol.*, 2023, **13**, 2223–2238.
- 21 J. C. Serrano-Ruiz, R. Luque and J. H. Clark, in *The Role of Catalysis for the Sustainable Production of Bio-fuels and Bio-chemicals*, eds. K. S. Triantafyllidis, A. A. Lappas and M. Stöcker, Elsevier, Amsterdam, 2013, pp. 557–576.
- 22 J. C. Serrano-Ruiz, R. Luque and A. Sepúlveda-Escribano, *Chem. Soc. Rev.*, 2011, **40**, 5266.
- 23 A. Choplin and F. Quignard, *Coordination Chemistry Reviews*, 1998, **178–180**, 1679–1702.
- 24 V. P. Zhdanov and B. Kasemo, *Journal of Catalysis*, 1997, **170**, 377–389.
- 25 D.-P. Yang, Z. Li, M. Liu, X. Zhang, Y. Chen, H. Xue, E. Ye and R. Luque, *ACS Sustainable Chem. Eng.*, 2019, **7**, 4564–4585.
- 26 S. Mao, C. Wang and Y. Wang, *Journal of Catalysis*, 2019, **375**, 456–465.
- 27 D. Polidoro, A. Perosa, E. Rodríguez-Castellón, P. Canton, L. Castoldi, D. Rodríguez-Padrón and M. Selva, *ACS Sustainable Chem. Eng.*, 2022, **10**, 13835–13848.
- 28 A. Samikannu, L. J. Konwar, P. Mäki-Arvela and J.-P. Mikkola, *Applied Catalysis B: Environmental*, 2019, **241**, 41–51.
- 29 H. Xu, S. Zhang, J. Geng, G. Wang and H. Zhang, *Inorganic Chemistry Frontiers*, 2021, **8**, 2829–2834.
- 30 M. Campanati, G. Fornasari and A. Vaccari, *Catalysis Today*, 2003, **77**, 299–314.
- 31 D. Polidoro, D. Rodríguez-Padrón, A. Perosa, R. Luque and M. Selva, *Materials*, 2023, **16**, 575.
- 32 M. J. Muñoz-Batista, D. Rodríguez-Padrón, A. R. Puente-Santiago and R. Luque, *ACS Sustainable Chem. Eng.*, 2018, **6**, 9530–9544.
- 33 L. Takacs, *Chem. Soc. Rev.*, 2013, **42**, 7649–7659.
- 34 S. Mateti, M. Mathesh, Z. Liu, T. Tao, T. Ramireddy, A. M. Glushenkov, W. Yang and Y. I. Chen, *Chem. Commun.*, 2021, **57**, 1080–1092.
- 35 F. Kh. Urakaev and V. V. Boldyrev, *Powder Technology*, 2000, **107**, 93–107.
- 36 L.-W. Zhan, L. Han, P. Xing and B. Jiang, *Org. Lett.*, 2015, **17**, 5990–5993.
- 37 N. G. C. Change, 10 interesting things about air,

- <https://climate.nasa.gov/news/2491/10-interesting-things-about-air>, (accessed September 18, 2023).
- 38 Selective oxidation of benzyl alcohols to benzaldehydes catalyzed by dioxomolybdenum Schiff base complex: synthesis, spectral characterization, crystal structure, theoretical and computational studies | SpringerLink, <https://link.springer.com/article/10.1007/s11243-021-00460-w>, (accessed September 15, 2023).
- 39 Iron(III) Nitrate/TEMPO-Catalyzed Aerobic Alcohol Oxidation: Distinguishing between Serial versus Integrated Redox Cooperativity | Journal of the American Chemical Society, <https://pubs.acs.org/doi/10.1021/jacs.1c05224>, (accessed September 15, 2023).
- 40 Understanding of the Oxidation Behavior of Benzyl Alcohol by Peroxymonosulfate via Carbon Nanotubes Activation | ACS Catalysis, <https://pubs.acs.org/doi/full/10.1021/acscatal.9b05273>, (accessed September 15, 2023).
- 41 A. F. Abdel-Magid, K. G. Carson, B. D. Harris, C. A. Maryanoff and R. D. Shah, *J. Org. Chem.*, 1996, **61**, 3849–3862.
- 42 O. I. Afanasyev, E. Kuchuk, D. L. Usanov and D. Chusov, *Chem. Rev.*, 2019, **119**, 11857–11911.
- 43 S. D. Roughley and A. M. Jordan, *J. Med. Chem.*, 2011, **54**, 3451–3479.
- 44 L. Jiang, P. Zhou, Z. Zhang, S. Jin and Q. Chi, *Ind. Eng. Chem. Res.*, 2017, **56**, 12556–12565.
- 45
- 46 Acetonitrile suitable for HPLC, gradient grade, ≥99.9% | Sigma-Aldrich, <https://www.sigmaaldrich.com/IT/it/product/sigald/34851>, (accessed September 15, 2023).
- 47
- 48 F. Rezaie, V. Pirouzfard and A. Alihosseini, *Thermal Science and Engineering Progress*, 2020, **16**, 100463.
- 49 R. Xia, D. Tian, S. Kattel, B. Hasa, H. Shin, X. Ma, J. G. Chen and F. Jiao, *Nat Commun*, 2021, **12**, 1949.
- 50 B. Coq, D. Tichit and S. Ribet, *Journal of Catalysis*, 2000, **189**, 117–128.
- 51 J. Andraos, *Org. Process Res. Dev.*, 2009, **13**, 161–185.
- 52 C. R. McElroy, A. Constantinou, L. C. Jones, L. Summerton and J. H. Clark, *Green Chem.*, 2015, **17**, 3111–3121.

- 53 P. N. Sharratt, in *Handbook of Batch Process Design*, ed. P. N. Sharratt, Springer Netherlands, Dordrecht, 1997, pp. 1–23.
- 54 D. Polidoro, C. Espro, N. Lazaro, O. Trentin, A. Perosa, S. M. Osman, D. Rodríguez-Padrón, R. Luque and M. Selva, *Catalysis Today*, 2023, **423**, 113890.
- 55 A. Fayeulle, E. Trudel, A. Damiens, A. Josse, N. Ben Hadj Youssef, P. Vigneron, M. Vayssade, C. Rossi and C. Ceballos, *Sustainable Chemistry and Pharmacy*, 2021, **22**, 100471.
- 56 E. A. Hoff, G. X. De Hoe, C. M. Mulvaney, M. A. Hillmyer and C. A. Alabi, *J. Am. Chem. Soc.*, 2020, **142**, 6729–6736.
- 57 C. S. Cho, B. T. Kim, T.-J. Kim and S. C. Shim, *Chem. Commun.*, 2001, 2576–2577.
- 58 PubChem, PubChem, <https://pubchem.ncbi.nlm.nih.gov/>, (accessed September 28, 2023).
- 59 F. Saberi, D. Rodriguez-Padrón, A. Garcia, H. R. Shaterian and R. Luque, *Catalysts*, 2018, **8**, 167.
- 60 A. P. Dicks and A. Hent, in *Green Chemistry Metrics: A Guide to Determining and Evaluating Process Greenness*, eds. A. P. Dicks and A. Hent, Springer International Publishing, Cham, 2015, pp. 1–15.